Understanding the mechanism for the low-temperature reduction of Fe$_2$O$_3$ to Fe in alkaline electrolytes

Raj Shekhar,[1] Semanti Mukhopadhyay,[2] Francelia Sanchez,[2] Anastasiia Konovalova,[1] Shannon W. Boettcher,[1,3] Arun Devaraj,[2] Paul A. Kempler[1*]

[1]*Department of Chemistry and Biochemistry and the Oregon Center for Electrochemistry, University of Oregon, Eugene, OR, USA*

[2]*Physical and Computational Sciences Directorate, Pacific Northwest National Laboratory, Richland, WA, USA*

[3] *Department of Chemical & Biomolecular Engineering and Department of Chemistry, University of California, and Energy Storage and Distributed Resources Division, Lawrence Berkeley National Laboratory, Berkeley, CA, USA*

*Correspondence: pkempler@uoregon.edu

Abstract:

Conversion reactions for iron oxide to iron metal enable zero-emissions iron for steelmaking and low-cost batteries for long duration energy storage. Iron oxides such as hematite can be electrochemically reduced to metallic iron in concentrated alkaline electrolytes at modest temperatures, but the influence of solid-state and dissolved intermediates at practical reaction rates remains unclear. Here we show that the inner morphology of hematite particles controls both their reactivity and apparent reduction mechanism. Correlated electron microscopy and rotating-ring-disk-electrode measurements revealed that porous particles proceed primarily through a dissolution-redeposition pathway, with small nanoparticles nucleating within a diffusion length of particles undergoing reductive dissolution. In contrast, dense hematite particles underwent reactive fracture to directly form iron metal. While previous studies on iron electrowinning have primarily focused on the role of particle diameter, these results demonstrate the importance of the dissolution-redeposition pathway for electrowinning processes and suggest that internal porosity controls iron oxide reactivity at temperatures < 100 °C. Iron-oxide-to-metal electrolyzers and fast-charging iron-air batteries supported by curtailed electricity can increase the rate of metal formation by accelerating dissolution in reactant oxides. Electrochemical milling of dense oxides leads to particles smaller than what is obtained using conventional milling and grinding methods.

Introduction:

Iron (Fe) metal is essential in modern society, and may soon play a substantial role in inexpensive, long duration energy storage systems.[1-3] Globally, the reduction of iron oxides to metal during primary steelmaking contributes ~7% of annual carbon dioxide emissions and potential decarbonized alternatives have yet to realize commercial operation.[4-7] The majority of these sector-wide emissions occur during the chemical reduction of processed iron ores (largely hematite, α-Fe_2O_3) in blast furnaces, with coal-derived CO serving as the reductant and CO_2 produced as the oxidized product (**equation 1**).[2]

$$Fe_2O_3 + 3\ CO \rightarrow 2\ Fe + 3\ CO_2 \tag{1}$$

These process CO_2 emissions can be avoided if Fe is reduced instead using zero-carbon electricity and water. For example, α-Fe_2O_3 can be directly reduced in water to form iron and hydroxide, OH^- (**equation 2**).[8,9]

$$2\ Fe_2O_3 + 3\ H_2O + 6\ e^- \rightarrow 4\ Fe + 6\ OH^- \tag{2}$$
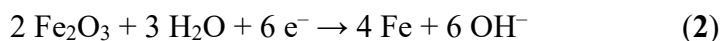
The reduction of H_2O to H_2 is a source of parasitic current as it is generally thermodynamically favorable compared to Fe formation (**equation 3**). This reaction occurs at the negative electrode of iron-air batteries, where controlling the selectivity between Fe and water reduction can limit the maximum charging rate.[3]
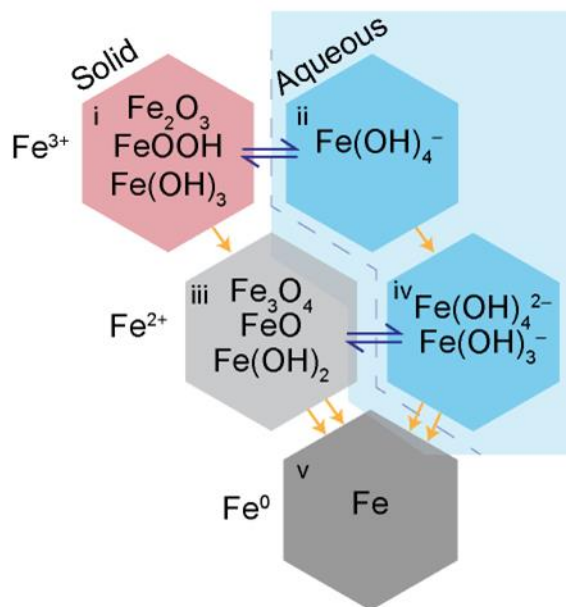
$$2\ H_2O + 2\ e^- \rightarrow H_2 + 2\ OH^- \tag{3}$$

Pathways for reducing α-Fe_2O_3 to Fe can be classified as all-solid-state or dissolution-redeposition mechanisms, with the latter requiring the presence of at least one soluble (aqueous) intermediate (**Scheme 1 ii, iv**). Although α-Fe_2O_3 is only sparingly soluble in concentrated OH^- electrolytes, the solubility of ferrous and ferric species increases at the temperatures commonly used in electrodeposition experiments (80–110 °C).[10,11] Trace quantities of dissolved intermediates

play an important role in geochemical processes involving α-Fe_2O_3.[12,13] Corrosion and redeposition of Fe in 20 M NaOH at 80–120 °C has been shown to support current densities, $J \sim 0.02$ A cm^{-2} with deposits resembling the dendritic morphology of those produced from hematite slurries.[14] The formation of dendrites at Fe films has previously been attributed to both solid-state and dissolution-redeposition mechanisms.[15,16]

Scheme 1: Chemical and electrochemical conversion reactions associated with the reduction of Fe_2O_3 to Fe at low temperatures. Solid-liquid equilibria are shown by blue arrows and electrochemical reduction steps are shown by yellow arrows.

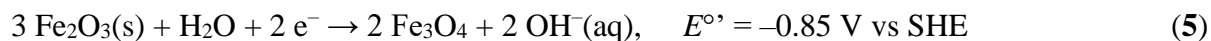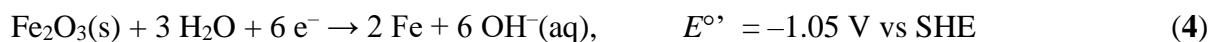Transport limitations could limit the role of sparingly soluble intermediates during Fe growth at current densities > 0.1 A cm^{-2}.[17,18] For this reason, many have suggested a reaction pathway that bypasses dissolved Fe species,[19,20] but the experimental evidence supporting a solid-state mechanism is incomplete. Magnetite (Fe_3O_4) and metallic Fe have been observed via *ex-situ* Mössbauer spectroscopy within reactant α-Fe_2O_3 particles following reduction at –1.2 V vs Hg/HgO in 50 wt.% NaOH at 100 °C, which seems to support a solid-state reaction pathway (**Scheme 1 i→iii→v**).[21] Moreover, epitaxial Fe_3O_4 films grown on Au convert to epitaxial Fe metal, but without direct measurements of intermediate products the mechanism could not be resolved.[19]

The formal potential, $E^{\circ\prime}$ is the most convenient thermodynamic descriptor for Fe_2O_3 to Fe reactions (**equation 4–6**) because the activity coefficient of OH$^-$ and H_2O is dependent on the cell temperature (as well other dissolved species) and is an important variable in concentrated and heated electrolytes relevant to energy storage and electrowinning.[22] The estimated $E^{\circ\prime}$ for various

solid state conversions assuming $[OH^-]$ = 10 M are provided in **equations 4–6**. (**Supplemental Information, Table S1, S2**)

$$Fe_2O_3(s) + 3\ H_2O + 6\ e^- \rightarrow 2\ Fe + 6\ OH^-(aq), \qquad E^{\circ\prime} = -1.05\ V\ vs\ SHE \qquad (4)$$

$$3\ Fe_2O_3(s) + H_2O + 2\ e^- \rightarrow 2\ Fe_3O_4 + 2\ OH^-(aq), \quad E^{\circ\prime} = -0.85\ V\ vs\ SHE \qquad (5)$$

$$Fe_3O_4 + 4\ H_2O + 8\ e^- \rightarrow 3\ Fe + 8\ OH^-(aq), \qquad E^{\circ\prime} = -1.07\ V\ vs\ SHE \qquad (6)$$

Dissolution-redeposition mechanisms will include at least one dissolved ferric/ferrous hydroxide couple,[14,23–25] with OH^- produced as the deoxygenation product (**equations 7–8**). We assume $Fe(OH)_4^{2-}(aq)$ to be the dominant ferrous species in concentrated hydroxide at $T < 100$ °C.[10] $E^{\circ\prime}$ for reactions involving dissolved iron species was calculated assuming $[Fe(OH)_4]^{2-}$ = $[Fe(OH)_4]^-$ = 1 mM although we note that the saturated concentration of both species is a function of the temperature, [NaOH], and electrode potential.[10,26]

$$Fe(OH)_4^-(aq) + e^- \rightarrow Fe(OH)_4^{2-}(aq) \qquad\qquad E^{\circ\prime} = -0.82\ V\ vs\ SHE \qquad (7)$$

$$Fe(OH)_4^{2-}(aq) + 2e^- \rightarrow Fe(s) + 4OH^-(aq) \qquad\qquad E^{\circ\prime} = -1.05\ V\ vs\ SHE \qquad (8)$$

Most experimental reports of the direct conversion of α-Fe_2O_3 primarily focus on commercial Fe_2O_3 powders,[8,24,27,28] but a few studies have used naturally occurring iron oxide ores that are predominately dense α-Fe_2O_3 with Fe_3O_4, silica, and alumina impurities, due to their practical relevance and abundance.[21] Pressed pellets of Fe_2O_3, Fe_3O_4, and mixed Fe-Al ceramics have been explored as cathodes for alkaline iron reduction,[29–31] where the micron-scale porosity within the bulk pellet has been shown to have a significant influence on the electrode kinetics. Studies of individual ore particles revealed geometric trends in the growth of Fe around the particle surface and apparent limits in conversion as a function of particle diameter.[21] Very little data exists, however, on the intrinsic reduction kinetics of fully-dense (ore-like) α-Fe_2O_3 particles in the absence of transport restrictions or impurities which influence the reaction selectivity.[32]

Furthermore, while the role of particle size has been frequently discussed,[20,21,25] the influence of nanoscale porosity has received less attention and is rarely quantified for reactant α-Fe_2O_3.

Fe negative electrodes generally limit the power density of secondary iron-air batteries for long-duration energy storage.[33,34] While electrodes for oxygen evolution and oxygen reduction can operate at high rates ($J > 0.10$ A cm^{-2}), Fe electrodes are most often cycled at $J < 0.05$ A cm^{-2} to avoid passivation by insulating oxide phases and parasitic hydrogen evolution.[34,35] The specific surface area and chemical composition of Fe electrodes evolve with repeated cycling,[36] and the lifecycle of these electrodes is believed to terminate with the formation of micron-scale γ-Fe_2O_3 crystals with low electrical conductivity. Dissolved Fe species have long been known to play an important role in charging/discharging mechanisms for secondary iron electrodes,[3,34,37,38] but measurements of dissolved intermediates within the cell environment are rarely reported.

In this study, we prepare a set of high-purity α-Fe_2O_3 precursors to investigate how the nanoscale morphology of oxides influences the mechanism and rate of metal-oxide-to-metal conversion reactions. Molten-salt annealing of synthetic α-Fe_2O_3 particles to prepare dense, micron-scale α-Fe_2O_3 phases enabled direct comparisons of porosity and reactivity at moderate temperatures. Rotating-ring-disk-electrode (RRDE) measurements were used to quantify the presence of dissolved Fe intermediates during electrowinning reactions for the first time. Correlated electron microscopy measurements revealed distinct ore-to-metal pathways that were influenced by the morphology of the reactant oxide, including a new form of electrochemical milling.

Results and Discussion

Characterization of α-Fe_2O_3 reactants

Hematite particles were first characterized via scanning electron microscopy (SEM), high-resolution transmission electron microscopy (HRTEM), powder X-ray diffraction (XRD), and Raman prior to electrochemical reduction (**Fig. 1**) Commercial α-Fe_2O_3 (*com*-Fe_2O_3) consisted of a polydisperse set of particles of variable morphology (**Fig. 1a**). The largest individual particles were ~200 nm diameter, but nanoparticles as small as 20 nm in diameter were present within agglomerates. These particles thus pose practical challenges for investigating reactions potentially controlled by surface area or solid-state diffusion. Therefore, we synthesized a set of homologous α-Fe_2O_3 particles having similar diameters but tunable morphology, following a previously reported method for synthesizing pseudo-cubic α-Fe_2O_3 (*pc*-Fe_2O_3, **Supplemental Information**).[39] A subset of these particles was heated at 1000 °C under N_2 atmosphere to produce annealed particles with only a few crystalline domains (*an*-Fe_2O_3).

As-prepared *pc*-Fe_2O_3 particles ranged in diameter from 0.2 to 0.9 µm with an average diameter of 0.5(1) µm ($N = 208$, **Fig. 1b, Fig. S1-S2)**. The larger *pc*-Fe_2O_3 particles visible in SEM were composed of smaller 15–25 nm α-Fe_2O_3 nanocrystals, as evident from transmission electron microscopy images (TEM, **Fig. 1b**, **Fig. S3)**. Particle size analysis of the diffraction data using the Scherrer equation indicated that the average crystalline domain size within *pc*-Fe_2O_3 particles was similar to the primary particle size observed via HRTEM (**Fig. 1b, Table S3**). After annealing, the size distribution of *an*-Fe_2O_3 particles was consistent with the precursor *pc*-Fe_2O_3 (**Fig. S4**), but the particles were faceted and nanocrystalline domains were no longer observed at the particle edges (**Fig. 1c, Fig. S5-S6, Table S4**).

Powder X–ray diffraction (**Fig. 1d**) and Raman spectroscopy (**Fig. 1e**) were used to compare the composition of the as-prepared Fe_2O_3 reactants. *Nat*-Fe_2O_3 particles yielded two small diffraction peaks at $2\theta = 25°$ and $57°$. A peak at $2\theta = 57°$ was also observed for *an*-Fe_2O_3 and was assigned to the (018) reflection of the hematite structure, with the absence of this feature in the
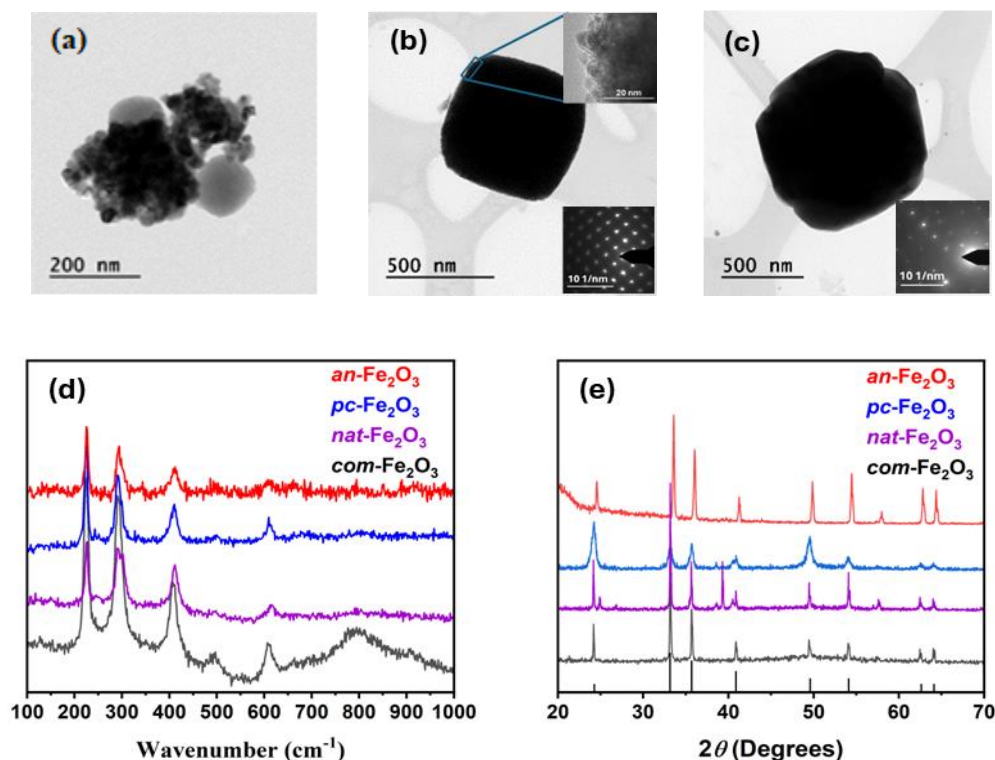

Figure 1: Dark field TEM images of **(a)** *com*-Fe_2O_3 particles **(b)** *pc*-Fe_2O_3 (upper and lower insets HRTEM image and SAED pattern, respectively **(c)** an-Fe_2O_3. **(d)** Powder XRD and **(e)** Raman spectra of *com*-Fe_2O_3, *nat*-Fe_2O_3, *pc*-Fe_2O_3, and *an*-Fe_2O_3.

diffraction patterns for *pc*-Fe_2O_3 and *com*-Fe_2O_3 attributed to reduced crystallinity within the particles. All iron-oxide samples yielded a similar set of peaks in their Raman spectra, except for two broad peaks observed for *com*-Fe_2O_3 at ~500 cm^{-1} and ~800 cm^{-1}, assigned to the A_{1g} mode and an amorphous impurity phase, respectively.[40] The relative intensities of the peaks at 225 cm^{-1} and 293 cm^{-1} were increased for *nat*-Fe_2O_3 relative to *pc*-Fe_2O_3 and *com*-Fe_2O_3 but comparable

for *an*-Fe$_2$O$_3$, which we attribute to the larger crystallite size of *nat*-Fe$_2$O$_3$ compared to other α-Fe$_2$O$_3$ particles.[40]

Ex-situ SEM and TEM analysis of α-Fe₂O₃ particles

Fig. 2 presents the chemical and morphological changes to α-Fe$_2$O$_3$ particles supported on polished, polycrystalline Au after electrochemical reduction in 10 M NaOH. The initial number density measured via SEM was ~15 particles per 100 µm^2 (**Fig. 2a,e**) but after reduction at –1.3 V for 5 min, the original *pc*-Fe$_2$O$_3$ particles were surrounded by 800 particles per 100 µm^2 of nanoparticles < 100 nm in diameter (**Fig. 2b**, **Fig. S7**). The fractional iron content (at%) measured via SEM energy dispersive x-ray spectroscopy (SEM-EDS) confirmed that the particles were deoxygenated from an initial composition consistent with Fe$_2$O$_3$ (40 at% Fe) to a final composition of 64 at% Fe (**Fig. S7, Table S5**). In contrast, similar treatment of *an*-Fe$_2$O$_3$ particles did not lead to the formation of visible nanoparticles via SEM or EDS on the Au substrate, (**Fig. 2e,f**), but a subset of particles fractured to form a small collection of nanoparticles with a high Fe at% in the same spatial area as the original *an*-Fe$_2$O$_3$ particle (**Fig. S8**).
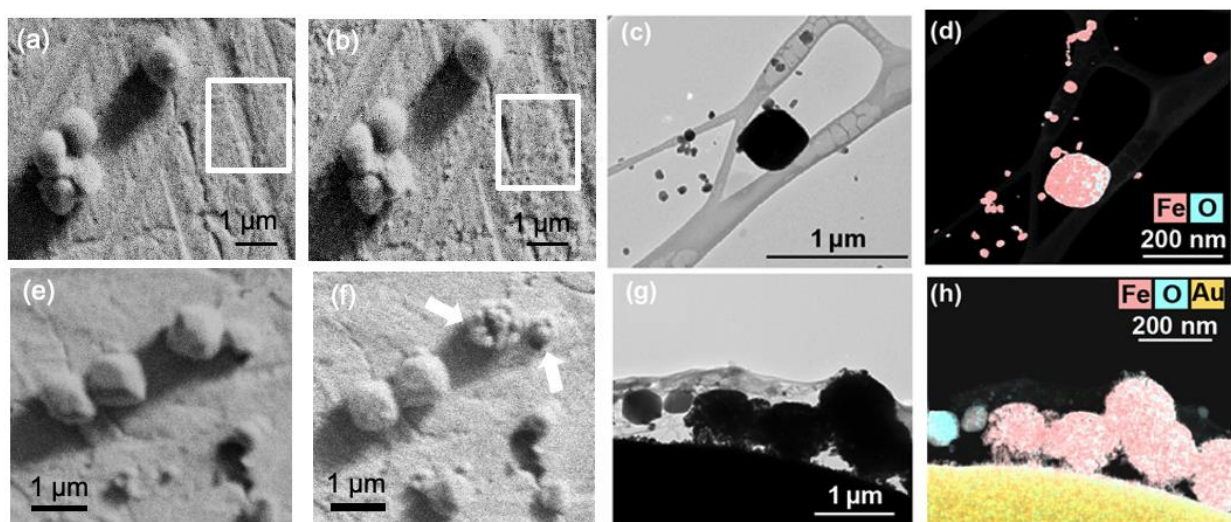
Figure 2: Representative correlated SEM images of **(a,b)** *pc*-Fe$_2$O$_3$ and **(e,f)** *an*-Fe$_2$O$_3$. A polycrystalline Au electrode was imaged **(a,e)** as-deposited and **(b,f)** after reduction. TEM-EDS images of **(c,d)** *pc*-Fe$_2$O$_3$ and **(g,h)** *an*-Fe$_2$O$_3$ after reduction. Reduction of the films occured at –1.3 V vs Hg/HgO in 30 wt.% NaOH in H$_2$O at 80 °C under N$_2$. A Au TEM grid served as a working electrode.

The structure and composition of the substrate-supported and Fe_2O_3-supported nanoparticles were characterized using dark-field TEM (**Fig. 2c,g**) and EDS mapping (**Fig. 2d,h**). Nanoparticles, 40–100 nm in diameter and having an Fe content of at least 80 at% Fe, were visible in the regions adjacent to parent *pc*-Fe_2O_3 particles (**Fig. 2c,d, Fig. S9**). While *an*-Fe_2O_3 particles supported on the TEM grid were all found to deoxygenate, only fractured particles exhibited elemental compositions with >90 at% Fe (**Fig. 2h**).

Cross sections of a fractured and unfractured *an*-Fe_2O_3 particle were further characterized used scanning transmission electron microscopy (STEM) and transmission Kikuchi diffraction (TKD), **Fig 3**. **Fig. 3a** displays a cross-section of a single, reduced and fractured *an*-Fe_2O_3 particle which was excised from the grid and prepared for TEM characterization using focused ion beam (FIB) after reducing at –1.3 V vs Hg/HgO. EDS mapping revealed that the fractured particle was
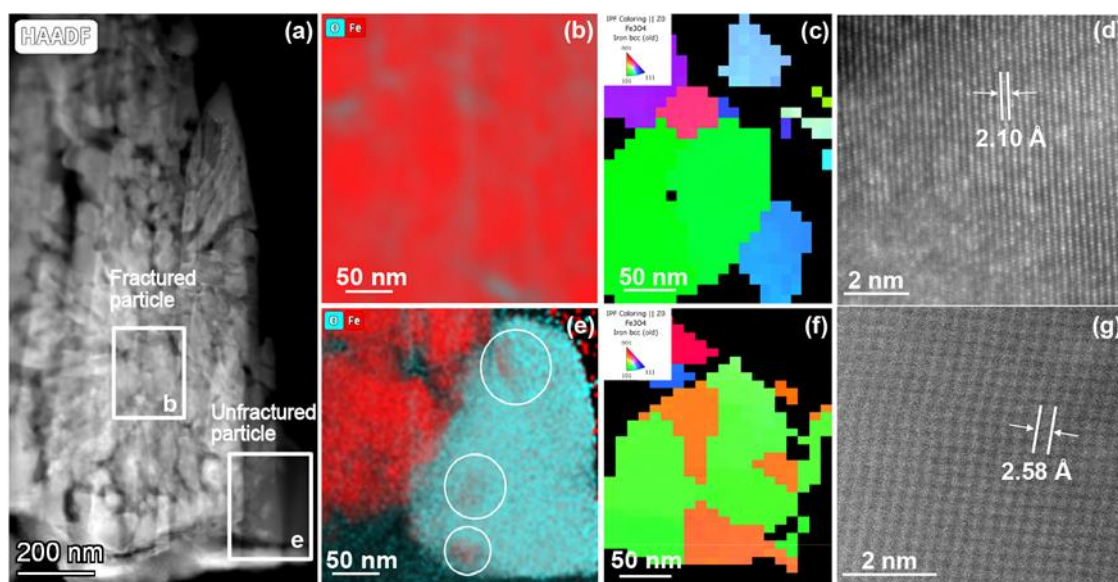
Figure 3: (a) HAADF-STEM image showing the cross-section of a fractured *an*-Fe_2O_3 and unfractured particle after reduction at –1.3 V in 30 wt.% NaOH. **(b)** EDS map showing Fe (in red) and O (in blue) content in the middle section of the fractured particle shown in (a). **(c)** TKD-based orientation map of fractured particle (b), **(d)** atomic-resolution HAADF-STEM micrograph of the fractured particle obtained along <110> zone axis (b). **(e)** EDS map of Fe and O content in the corner section of the unfractured particle shown in (a). **(f)** TKD-based orientation of unfractured particle (e), **(g)** atomic-resolution HAADF-STEM micrograph of the unfractured particle obtained along <311> zone axis (e).

almost completely deoxygenated except for a thin layer of oxide present along fissures, which we attribute to a passivation layer formed during transfer (**Fig. 3b, Fig. S10**). Similar behavior was observed across multiple Fe_2O_3 particles reduced on TEM grids although some particles were partially deoxygenated but did not fracture (**Fig. S11**). Analysis of inverse pole figure maps (IPF, **Fig. 3c**) acquired using TKD mapping (**Fig. S12**) indicated that the particles were bcc-Fe with random lattice orientations with respect to the electrode surface normal. The d-spacing calculated from zone axis high-angle annular dark field (HAADF) micrographs also confirmed the presence of bcc-Fe (**Fig. 3d**). TKD and HAADF-STEM imaging of a partially reacted particle (**Fig. S13**) adjacent to the fractured Fe particle revealed a cubic inverse spinel structure, which could be assigned to Fe_3O_4 however, the presence of γ-Fe_2O_3 could not be ruled out. EDS mapping of this partially reacted particle revealed nm-scale Fe-rich domains (marked circles) within a predominately Fe_3O_4 particle (**Fig. 3e,f**), as supported by TKD measurements (**Fig. S13**) and the d-spacing of lattice fringes (**Fig. 3g**).

Thin film voltammetry of α-Fe₂O₃

We next employed thin-film voltammetry to probe the electrochemical steps involved in the multielectron reduction of α-Fe_2O_3. The mass-loading of Fe_2O_3 was held constant across experiments (43 µg cm^{-2}) and was selected to produce sub-monolayer films of particles on glassy carbon, which minimized the influence of water reduction and localized the current response to particles in direct electrical contact with the electrode (**Fig. S14**). Reduction of α-Fe_2O_3 yielded morphology-dependent current-voltage (*i-E*) responses in 10 M NaOH during the first cyclic voltammogram at 5 mV s^{-1} (**Fig. 4**).

The onset of cathodic current ($E < -0.9$ V) occurred earlier for *pc*-Fe_2O_3 compared to *an*-Fe_2O_3 ($E < -1.17$ V). The *pc*-Fe_2O_3 voltammetry also featured two distinct cathodic waves with a

peak gravimetric current of –1.2 A g^{-1} at $E_p = -1.17$ V, whereas only a single cathodic wave, lacking a well-resolved peak, was measured at *an*-Fe$_2$O$_3$ films (**Fig. 4b**). The integrated cathodic charge for Fe reduction, Q_{Fe}, was calculated from the current prior to the onset of water reduction (**equation 9**),

$$Q_{Fe} = 1/v \int_{-0.9}^{-1.2} i \, dE \tag{9}$$

where *v* represents the scan rate. Q_{Fe} was 4 mC and 0.8 mC for the *pc*-Fe$_2$O$_3$ and *an*-Fe$_2$O$_3$ particles, respectively, which was sufficient to reduce 37% and 7% of the initial Fe$_2$O$_3$ loading, based on a three-electron reduction. Qualitatively similar trends in voltammetry were observed across *com*-Fe$_2$O$_3$ and *pc*-Fe$_2$O$_3$, with both samples yielding two separate reduction waves with a peak gravimetric current of –0.5 A g^{-1} at $E_p = -1.16$ V (**Fig. 4b**). Q_{Fe} for *com*-Fe$_2$O$_3$ was 30%. A thin film prepared from natural Fe$_2$O$_3$ (*nat*-Fe$_2$O$_3$, **Fig. S15**) showed the lowest activity of all particles, despite the presence of nanometer-scale fines, with an onset of cathodic current at $E < -1.17$ V. Although water reduction at $E < -1.2$ V prevented measurements of Fe reduction kinetics, the
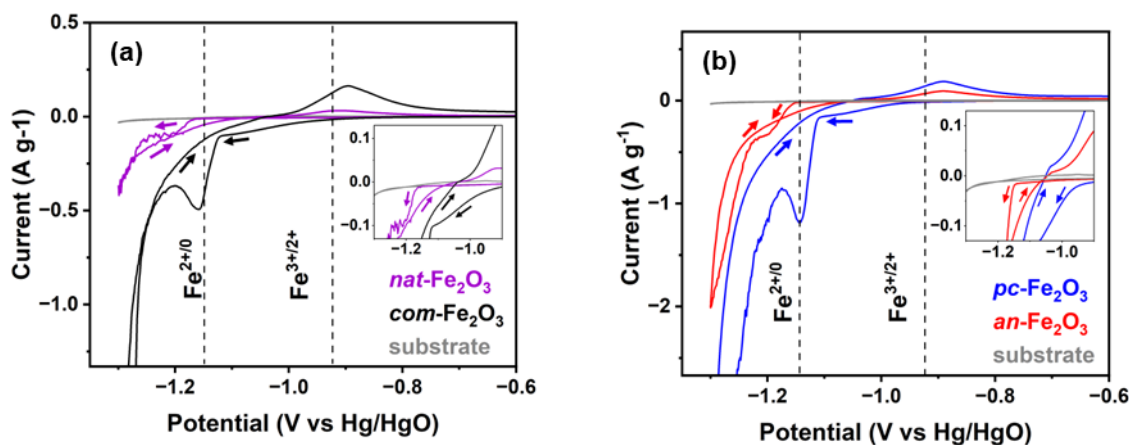
Figure 4: Voltammetry of glassy carbon electrode and glass carbon electrodes modified with thin films of (a) *nat*-Fe$_2$O$_3$ and *com*-Fe$_2$O$_3$ and (b) *pc*-Fe$_2$O$_3$ and *an*-Fe$_2$O$_3$ in 30 wt.% NaOH at 80 °C at $v = 5$ mV s^{-1}. The mass loading of Fe$_2$O$_3$ was 43 μg cm^{-2} for all electrodes. The formal potential for reactions (1) and (2) are indicated with the dotted line. The formal potential, $E°'$, for Fe(OH)$_4^{-/2-}$ as well as Fe(OH)$_4^{2-}$ reduction to Fe(s) in 30 wt.% NaOH at 80 °C are indicated as dashed lines at $E = -0.92$ V and -1.14 V vs Hg/HgO, respectively.

oxidation of a reduced Fe species was evident in the positive return sweep for all particles. and substantially more reversible charge towards Fe was passed for *com*-Fe₂O₃ and *pc*-Fe₂O₃ compared to *nat*-Fe₂O₃ and *an*-Fe₂O₃ (**Supplementary Information**).

Thin film RRDE of α-Fe₂O₃ samples

We used a rotating ring disk electrode (RRDE) to directly quantify the role of dissolved Fe^{3+} and Fe^{2+} intermediates. A glassy-carbon ring electrode allowed for the selective oxidation of Fe^{2+} over competing H_2 oxidation and thus was used to continuously monitor the rate of formation of soluble Fe^{2+} (**Supplemental Information**). **Figure 5a** presents the voltametric response of thin film *com*-Fe₂O₃, *pc*-Fe₂O₃, and *an*-Fe₂O₃ during rotation at 1000 rpm in 30 wt.% NaOH at 80 °C. During continuous forced convection, *pc*-Fe₂O₃ and *com*-Fe₂O₃ films no longer produced substantial cathodic currents at $E > -1.0$ V and also did not show a clearly resolved current maximum. However, the onset of Fe^{3+} reduction was apparent at the ring, which showed an onset of Fe^{2+} formation at
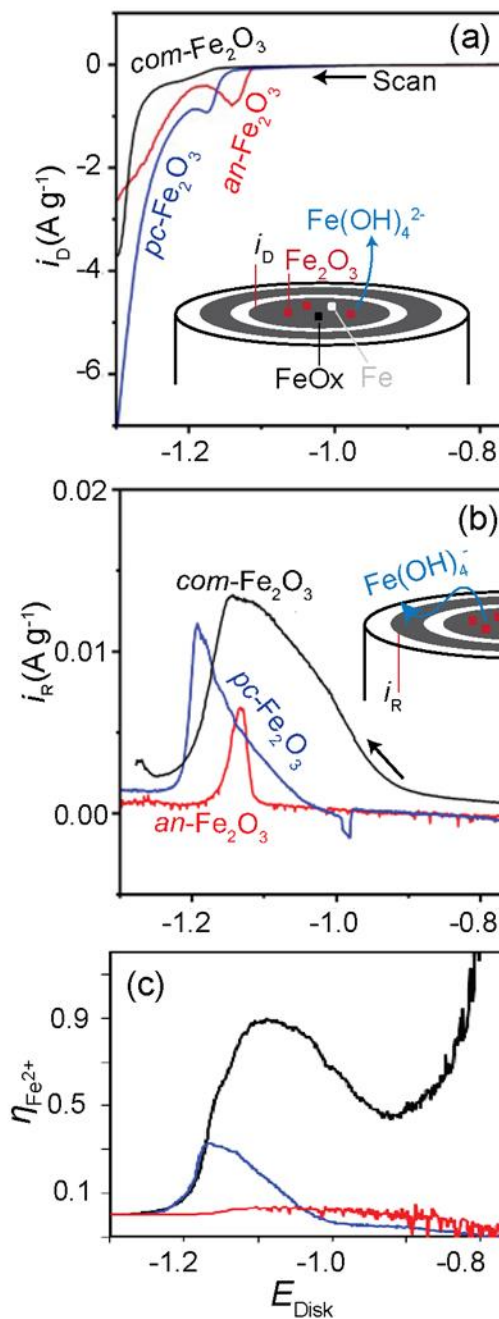
Figure 5: RRDE of thin films Fe₂O₃ in 30 wt.% NaOH at 80 °C. **(a)** disk current during negative sweep **(b)** ring current ring **(c)** The fraction of soluble Fe^{2+} ($\eta_{Fe^{2+}}$) formation. Scan rate = 5 mV s⁻¹. Rotation rate = 1000 rpm. The potential of the ring was held at –0.3 V vs. Hg/HgO throughout. Initial Fe₂O₃ loading = 43 µg cm⁻².

$E < -0.93$ V and -1.0 V, for *com*-Fe_2O_3 and *pc*-Fe_2O_3 particles, respectively (**Fig. 5c**). In contrast, *an*-Fe_2O_3 films yielded a previously unresolved cathodic peak at $E_p = -1.15$ V but a similar, gradual onset in i_R at $E > -1.1$ V was not observed. Instead, as a sharp peak i_R occurred at $E = -1.15$ V. For all particles, i_R approached 0.0 mA cm^{-2} for $E < -1.2$ V.

The current efficiency towards soluble Fe^{2+} species ($\eta_{Fe^{2+}}$) which could be detected at the ring was calculated as (**equation 10**)

$$\eta_{Fe^{2+}} = \frac{i_R}{i_D N_c} \tag{10}$$

where, N_c is the collection efficiency (36 ± 4 %) calibrated in 30 wt.% NaOH using $Ru^{2+/3+}$ (as $RuCl_3$) as a soluble and facile redox couple in alkali (**Fig. S16**). The fraction of soluble Fe^{2+} collected was highest for *com*-Fe_2O_3 and was near zero for *an*-Fe_2O_3 particles. The maximum value of $\eta_{Fe^{2+}}$ for *com*-Fe_2O_3 particles occurred at $E = -1.08$ V where $\eta_{Fe^{2+}}$ 89% (**Fig. 5d**), where a majority of the current could be assigned to reductive dissolution. The maximum value of $\eta_{Fe^{2+}}$ for the *pc*-Fe_2O_3 was 33% at $E = -1.15$ V and 3% for *an*-Fe_2O_3 at $E = -1.13$ V. In this potential region, both i_R and i_D increased slightly with increasing rotation rates (**Fig. S17**). This finding is inconsistent with mechanisms involving a dissolved intermediate that promotes reductive dissolution. Similar ring-disk electrodes measurements with 50 wt% NaOH serving as the supporting electrolyte led to a >15-fold increase in i_D and a limiting current was observed for $E >$ -1.15 V (**Fig. S18**) with further increases to i_D at $E < -1.15$ V leading to the disappearance of Fe^{2+} at the ring.

Measurements of Fe^{2+} during the positive sweep (**Fig. S19a**), revealed that oxidation of Fe to Fe^{2+} occurred at $E > -0.9$ V and Fe^{2+} was no longer detected for $E > -0.80$ consistent with the formation of Fe^{3+} and/or insoluble Fe^{2+} oxides or hydroxides. When the ring electrode was biased to reduce Fe^{3+}, a cathodic wave was observed (**Fig. S19b**) indicating the presence of soluble Fe^{3+}.

The oxidation current measured on the positive return sweep was highest for Fe films produced from pc-Fe_2O_3 followed by an-Fe_2O_3 and com-Fe_2O_3 particles. The amount of Fe^{2+} collected for the pc-Fe_2O_3 at the ring is also double that measured for an-Fe_2O_3 and com-Fe_2O_3 particles.

Discussion

Morphology and electrochemical activity of synthesized particles

Porous α-Fe_2O_3 and dense α-Fe_2O_3 particles having similar particle diameters facilitated quantitative comparisons of the influence of nanoscale porosity on electrochemical activity. Both pc-Fe_2O_3 and com-Fe_2O_3 shared qualitative similarities in morphology that are related to their recent precipitation from dissolved species, whereas an-Fe_2O_3 particles were more representative of compacted particles, which simulated distinct structural signatures of nat-Fe_2O_3 (**Fig. 1d**). Thin films of pc-Fe_2O_3 and com-Fe_2O_3 were reduced at the most positive E in the absence of forced convection, whereas an-Fe_2O_3 and nat-Fe_2O_3 particles were electrochemically inert for $E > -1.0$ V (**Fig. 4a–b**). All particles produced cathodic currents at $E < -1.1$ V, but a cathodic current peak was only observed for pc-Fe_2O_3 and com-Fe_2O_3. We assign this peak to reductive dissolution of α-Fe_2O_3 which can lead to Fe plating from $Fe(OH)_4{}^{2-}$ based on the onset potential. Activity towards reductive dissolution appears to be strongly sensitive to the presence of nanoscale porosity.

Correlated SEM and TEM images before and after electrochemical reduction at potentials sufficient to reduce α-Fe_2O_3 to Fe metal support a dissolution-redeposition mechanism for pc-Fe_2O_3 (**Fig. 2, 3**). The Fe-rich particles, 40–100 nm in diameter, observed in the vicinity of parent particles (**Fig. 2b,c**) were larger than the primary particles observed via SEM (15–25 nm, **Fig. S3, Fig. S9),** and thus could not have been formed via direct conversion of primary α-Fe_2O_3 since the α-Fe_2O_3 phase is 33% more dense compared to bcc α-Fe. The absence of any particles having $d < 25$ nm is thus evidence of Fe metal formation via dissolved ferrous species.

In contrast, oxides (Fe_3O_4 or γ-Fe_2O_3) and α-Fe were observed within the original phase boundaries of *an*-Fe_2O_3 particles as indicated by the TKD (**Fig. S12, S13c**) and EDS mapping (**Fig. 3e and Fig. S10, S13**). Formation of α-Fe was always accompanied by particle fracture, with intact particles showing increased O content (Fe:O = 4:1, **Fig. S11**). Particle fracture was positively correlated with larger particle diameters, which is suggestive of a stress-related mechanism driven by density differences in reduced oxides and metallic phases.[41,42] This represents a form of "electrochemical milling" which can drive size reduction in particles which too small to be processed by conventional grinding and milling equipment. Small Fe metal domains were observed in the same region as a larger partially reduced Fe_3O_4 phase, consistent with a mechanism where metal formation precedes fracture (**Fig. 3e**).

Dissolved species during Fe_2O_3 reduction

The earlier onset of cathodic ring current ($E > -1.1$ V) for *pc*-Fe_2O_3 and *com*-Fe_2O_3 particles indicates that these oxides more readily form dissolved ferrous species. Because the disk current in this region is mostly insensitive to potential, but diminished with transport of dissolved species away from the electrode surface, we assign this potential region to a dissolution-and-reduction mechanism (**Scheme 1 i→ii→iv→v, equation 11, Fig. S20**). The dissolution-and-reduction mechanism is consistent with the observation of a greater limiting current when Fe_2O_3 is suspended in 50 wt.% NaOH (**Fig. S18**) due to the increasing solubility of ferrous with increasing [OH^-].

$$Fe_2O_3 + 2\ OH^- + 3\ H_2O \rightarrow 2\ Fe(OH)_4^- \tag{11a}$$

$$Fe(OH)_4^- \rightarrow Fe(OH)_4^{2-} \tag{11b}$$
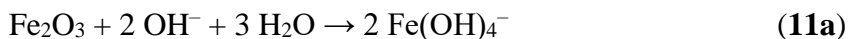
The current response in this region is inconsistent with a reductive–dissolution (**Scheme 1 i→iii→iv→v**) mechanism where removal of the dissolved intermediate would be expected to accelerate the chemical dissolution.

Greater than 65% of the charge passed at pc-Fe_2O_3 led to ferrous species which were not detected at the ring electrode (**Fig. 5d**). We attribute this irreversible charge, occurring at E positive of that necessary for Fe metal formation, to be the result of the formation of solid $Fe^{2+/3+}$ oxides, either directly (**Scheme 1 i→iii**) or via dissolution and redeposition (**Scheme 1 i→ii→iv→iii**) onto the Au electrode surface. For $E < -1.16$ V, Fe metal is expected to be the predominate species at the electrode surface and cathodic charge passed will lead to direct metal formation or indirectly capture dissolved ferrous species at adjacent Fe nuclei. This behavior is evident in the loss of i_R and $\eta_{Fe^{2+}}$ commensurate with the increase in $|i_D|$ (**Fig. 5c, d**).
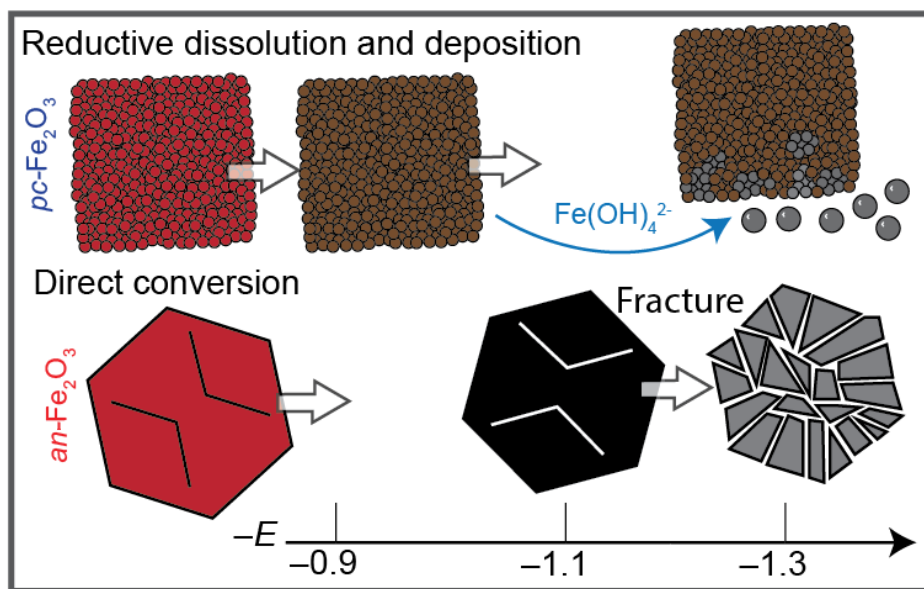
Scheme 2: Summary of Fe_2O_3 conversion mechanisms observed for pc-Fe_2O_3 and an-Fe_2O_3.

Cathodic currents that were present for pc-Fe_2O_3 and com-Fe_2O_3 particles at $E > -1.1$ V in stagnant cells were diminished to $i < 0.05$ A g^{-1} during electrode rotation at 1000 rpm. Consistent with previous reports,[8] we assign these currents to the electrochemical reduction of dissolved Fe^{3+}

species, which would accumulate in the stagnant boundary-layer for a thin film, but are rapidly removed from the surface by forced electrolyte convection driven by rotation (**Fig. S21**). Nevertheless, for *pc*-Fe_2O_3 particles, the rate of Fe^{2+} formation prior to solid state reduction is >10-fold less than the peak current for Fe metal formation in the absence of forced convection (**Fig. 5a, c**).

Comparisons to previous models for ore-to-metal processes

We observe four major differences in the apparent mechanism for α-Fe_2O_3 reduction in alkaline media relative to previously reported mechanisms (**Scheme 2**). First, we use RRDE measurements to find that for all Fe_2O_3 particles, soluble ferrous species are present within the reactive boundary layer during the onset of Fe formation (**Fig. 5c**). This does not rule out the presence of a solid-state conversion mechanism, but is the first evidence that soluble intermediates are consistently present during the initial stages of α-Fe_2O_3 reduction. Apparent solid-state reduction mechanisms may still be mediated by trace dissolved intermediates which travel nanometer length scales between dissolving oxides and growing metal phases.[12] Second, for dense, ore-like particles, the Fe_2O_3-to-Fe pathway occurs primarily via an *apparent* solid-state reduction of particles (**Fig. 2h, 3e**), with fracturing particles strongly correlated with the formation of Fe. The presence of small Fe domains within intact oxide phases is suggestive of fracture induced by Fe growth; further studies are necessary to understand the mechanics of this process. Third, mechanisms of α-Fe_2O_3 reduction involving an initial non-faradaic dissolution step forming $Fe(OH)_4^-$ appear to be inconsistent with the observed rates of Fe formation during electrowinning, as the transport-limited rate measured for ferric to ferrous reduction (**Fig. 5a,b**) is substantially smaller than the rate of reductive dissolution and/or iron metal formation (**Fig. 4**). Lastly, RRDE measurements suggest that dissolved ferrous species do not promote reductive dissolution of solid

α-Fe$_2$O$_3$ (**Fig. S17**), but oxide dissolution may be accelerated during the formation of Fe due to the consumption of dissolved ferrous intermediates (**Fig. 5**), and the fracture of low-surface area oxide particles (**Fig. 3a**).

Implications for electrowinning and energy storage:

Nanosized domains of α-Fe$_2$O$_3$ show substantially greater activity for reductive dissolution followed by plating (**Scheme 1 i→iii→iv→v**), compared to dense Fe$_2$O$_3$ particles (**Fig. 4**) which primarily form Fe via an *apparent* solid-state pathway coupled to reactive fracture (**Fig. 3**). XRD and Raman spectra provide useful spectroscopic signatures and information about crystallite size and crystal structure that are correlated with reactivity trends (**Fig. 1d,e**). These findings are consistent with studies showing increased activity during repeated potential-cycling is correlated with particle fragmentation leading to increased surface area.[3,36,43] Our results suggest that reactive fracture of insulating Fe$_2$O$_3$ phases (**Fig. 3a, Scheme 2**) at temperatures greater than typical cycling temperatures is one potential strategy to reactivate Fe electrodes suffering from capacity fade related to the formation of large, insulating iron oxide domains.[36]

The consistent presence of a dissolved ferrous species during the overall metal-forming reaction implies that accelerating oxide dissolution and increasing the solubility of the Fe^{2+} couple—via increased temperature, pH, or the addition of complexing agents—are possible desirable process modifications for increased rates of iron electrowinning and fast-charging Fe electrodes. Most natural iron oxides are mined as large particles of dense Fe$_2$O$_3$, which are different from the morphologies showing the greatest activity for Fe electrowinning here (**Fig. 4**).[32] New strategies for increasing the nanoscale porosity in oxide powders—including electrochemical milling as demonstrated here for *an*-Fe$_2$O$_3$—can enable the electrowinning of iron ores to metal in alkaline electrolytes at practical rates of reaction.

Conclusions:

The electrochemical activity of hematite at T <100 °C is substantially influenced by the nanoscale morphology of the reactant particle, with different α-Fe$_2$O$_3$ particles of consistent particle diameter proceeding through distinct reduction pathways to Fe metal. α-Fe$_2$O$_3$ particles with nanoscale pores follow a primarily dissolution–redeposition pathway leading to the formation of nanocrystalline Fe in the vicinity of partially reduced parent particles. On the other hand, annealed α-Fe$_2$O$_3$ particles with comparably low specific surface area and increased crystallinity were largely inert until the occurrence of particle fracture, presumably driving by partial reduction-induced mechanical stresses, which led to direct and essentially complete conversion from oxide to metal. The observation of rapid and complete reduction of annealed α-Fe$_2$O$_3$ particles to Fe after electrochemically-induced fracture provides a new strategy to activating naturally occurring Fe$_2$O$_3$ for decarbonized ironmaking.

Experimental methods:

Deionized water (DI H$_2$O) having a resistivity ≥18.1 MΩ-cm was obtained from a Millipore deionization system. α-Fe$_2$O$_3$ (98%, metals basis) and ferric chloride hexahydrate (FeCl$_3$·6H$_2$O, 97%) were obtained from Thermo Scientific. Sodium hydroxide (NaOH, 50 wt.%) was obtained from Fisher Chemical. A naturally-occurring α-Fe$_2$O$_3$ powder (*nat*-Fe$_2$O$_3$) was prepared by pulverizing a hematite specimen in a mortar and pestle selecting the $-$ 325 mesh fraction. α-Fe$_2$O$_3$ particles were prepared following a previously reported procedure involving a sol-gel synthesis followed by annealing in a molten-salt flux.[39]

Powder diffraction patterns of iron-oxide precursors were collected with a Bruker D2 phaser using a Cu-K*a* source (1.54 Å) with a step size of 0.02° and a 20–70° 2θ range. Raman spectra were collected using a Renishaw Raman microscope equipped with a 1 mW 633 nm red

laser as an excitation source and spectra were collected over 10 acquisitions. Microstructural analysis was performed by scanning electron microscopy (SEM, Thermo Fischer Apreo 2) using an accelerating voltage of 5–15 keV. Transmission electron microscopy (TEM) was performed on an FEI Titan 80-300 microscope at an accelerating voltage of 300 kV.

Thin films of α-Fe_2O_3 were prepared by drop casting 12 mM (Fe basis) suspensions of particles in DI H_2O onto electrodes and dried for 7 min under heat from an infrared lamp. Particles were dispersed via horn sonication (SX Ultrasonics) and redispersed in a bath sonicator prior to drop casting. Samples for TEM were prepared by drop casting the same α-Fe_2O_3 suspension onto a Cu/Au TEM grid (Ted Pella).

A Thermo Fisher Scientific Helios 600 Nanolab dual beam FIB-SEM was used to prepare a cross-sectional sample from a broken and unbroken *an*-Fe_2O_3 particle and thinned to electron transparency for further characterization. Transmission Kikuchi diffraction (TKD) was performed on this sample using the Helios Hydra UX dual beam plasma focused ion beam/ scanning electron microscope (PFIB/SEM) equipped with an Oxford Symmetry S2 detector. For this purpose, a 30 kV accelerating voltage at 13 nA were used to generate Kikuchi patterns, which were subsequently analyzed using Oxford AztecCrystal software.

In addition, a Themis Z 30-300 kV, Monochromated Aberration Corrected Transmission Electron Microscope operated at 300 kV was used for STEM and STEM-EDS on the cross-sectional FIB sample. Screen current of 60 pA and 1 nA were used for HAADF-STEM imaging and STEM-EDS mapping, respectively. STEM-EDS maps were acquired at 512 X 512 resolution with a 20 μs dwell time until a minimum of 100,000 counts were collected for each element. Further image processing and analyses were conducted using the Velox software.

Nickel wire (600 Ni, Malin Co.) served as the counter electrode while a Hg/HgO electrode filled with 30 wt.% NaOH served as the reference and was measured at 0.926 V vs RHE at 80 °C. A rotating-ring-disk electrode assembly, with glassy-carbon serving as both the disk and ring electrodes, was controlled by a BlueRev RC-10k (BioLogic). All electrochemical experiments were conducted with a Biologic SP-200 potentiostat. A 35 mL polypropylene container (Nalgene) served as the electrochemical cell. NaOH solutions were diluted to 30 wt.% with DI H_2O and purged with N_2 for at least 30 min before experiments.

Acknowledgements

References

1. Woodford, W. H., Burger, S., Ferrara, M. & Chiang, Y.-M. The iron-energy nexus: A new paradigm for long-duration energy storage at scale and clean steelmaking. *One Earth* vol. 5 212–215 (2022).

2. Fan, Z. & Friedmann, S. J. Low-carbon production of iron and steel: Technology options, economic assessment, and policy. *Joule* **5**, 829–862 (2021).

3. Manohar, A. K. *et al.* A High-Performance Rechargeable Iron Electrode for Large-Scale Battery-Based Energy Storage. *Journal of The Electrochemical Society* vol. 159 A1209–A1214 (2012).

4. Raabe, D., Tasan, C. C. & Olivetti, E. A. Strategies for improving the sustainability of structural metals. *Nature* vol. 575 64–74 (2019).

5. Zheng, X. *et al.* Correlating chemistry and mass transport in sustainable iron production. *Proc. Natl. Acad. Sci. U.S.A.* **120**, e2305097120 (2023).

6. Ma, Y. *et al.* Reducing Iron Oxide with Ammonia: A Sustainable Path to Green Steel. *Advanced Science* **10**, 2300111 (2023).

7. Allanore, A., Yin, L. & Sadoway, D. R. A new anode material for oxygen evolution in molten oxide electrolysis. *Nature* vol. 497 353–356 (2013).

8. Leduc, J. A. M., Loftfield, R. E. & Vaaler, L. E. Electrolytic Iron Powder from a Caustic Soda Solution. *Journal of The Electrochemical Society* vol. 106 659 (1959).

9. Allanore, A., Lavelaine, H., Valentin, G., Birat, J. & Lapicque, F. Iron metal production by bulk electrolysis of iron ore particles in aqueous media. *Journal of the Electrochemical Society* vol. 155 E125 (2008).

10. Beverskog, B. & Puigdomenech, I. Revised pourbaix diagrams for iron at 25–300 C. *Corrosion Science* **38**, 2121–2135 (1996).

11. Demnitz, M. *et al.* Effect of iron addition to the electrolyte on alkaline water electrolysis performance. *iScience* **27**, 108695 (2024).

12. Yanina, S. V. & Rosso, K. M. Linked Reactivity at Mineral-Water Interfaces Through Bulk Crystal Conduction. *Science* **320**, 218–222 (2008).

13. Putnis, A. & Putnis, C. V. The mechanism of reequilibration of solids in the presence of a fluid phase. *Journal of Solid State Chemistry* **180**, 1783–1786 (2007).

14. Allanore, A., Lavelaine, H., Valentin, G., Birat, J. P. & Lapicque, F. Electrodeposition of Metal Iron from Dissolved Species in Alkaline Media. *Journal of The Electrochemical Society* vol. 154 E187 (2007).

15. Majid, A. I., Finotello, G., van der Schaaf, J., Deen, N. G. & Tang, Y. On the formation of dendritic iron from alkaline electrochemical reduction of iron oxide prepared for metal fuel applications. *Chemical Engineering Science* **291**, 119931 (2024).

16. Zou, X. *et al.* Facile electrodeposition of iron films from $NaFeO_2$ and Fe_2O_3 in alkaline solutions. *Journal of The Electrochemical Society* **162**, D49 (2014).

17. Yuan, B., Kongstein, O. E. & Haarberg, G. M. Electrowinning of Iron in Aqueous Alkaline Solution Using a Rotating Cathode. *Journal of The Electrochemical Society* vol. 156 D64 (2009).

18. Tokushige, M., Kongstein, O. E. & Haarberg, G. M. Crystal Orientation of Iron Produced by Electrodeoxidation of Hematite Particles. *ECS Trans.* **50**, 103 (2013).

19. He, Z., Gudavarthy, R. V., Koza, J. A. & Switzer, J. A. Room-temperature electrochemical reduction of epitaxial magnetite films to epitaxial iron films. *Journal of the American Chemical Society* vol. 133 12358–12361 (2011).

20. Haarberg, G. M. & Yuan, B. Direct electrochemical reduction of hematite pellets in alkaline solutions. *ECS Transactions* vol. 58 19 (2014).

21. Allanore, A. *et al.* Observation and modeling of the reduction of hematite particles to metal in alkaline solution by electrolysis. *Electrochimica Acta* vol. 55 4007–4013 (2010).

22. Hausmann, J. N., Traynor, B., Myers, R. J., Driess, M. & Menezes, P. W. The pH of Aqueous NaOH/KOH Solutions: A Critical and Non-trivial Parameter for Electrocatalysis. *ACS Energy Lett.* **6**, 3567–3571 (2021).

23. Schwertmann, U. Solubility and dissolution of iron oxides. *Plant Soil* **130**, 1–25 (1991).

24. Boehme, C., Starykevich, M., Constantinescu, G., Kovalevsky, A. V. & Lopes, D. V. Low-Temperature Electrowinning of Iron from Mixed Hematite-Magnetite Alkaline Suspensions. *J. Electrochem. Soc.* **170**, 052502 (2023).

25. Lopes, D. V., Quina, M. J., Frade, J. R. & Kovalevsky, A. V. Prospects and challenges of the electrochemical reduction of iron oxides in alkaline media for steel production. *Frontiers in Materials* **9**, 1010156 (2022).

26. Allanore, A., Lavelaine, H., Valentin, G., Birat, J. P. & Lapicque, F. Electrodeposition of Metal Iron from Dissolved Species in Alkaline Media. *J. Electrochem. Soc.* **154**, E187 (2007).

27. Siebentritt, M., Volovitch, P., Ogle, K. & Lefèvre, G. Adsorption and electroreduction of hematite particles on steel in strong alkaline media. *Colloids and Surfaces A: Physicochemical and Engineering Aspects* **440**, 197–201 (2014).

28. Zou, X. *et al.* Electroreduction of Iron(III) Oxide Pellets to Iron in Alkaline Media: A Typical Shrinking-Core Reaction Process. *Metall Mater Trans B* **46**, 1262–1274 (2015).

29. Monteiro, J. F., Ivanova, Yu. A., Kovalevsky, A. V., Ivanou, D. K. & Frade, J. R. Reduction of magnetite to metallic iron in strong alkaline medium. *Electrochimica Acta* **193**, 284–292 (2016).

30. Ivanova, Yu. A. *et al.* Designed porous microstructures for electrochemical reduction of bulk hematite ceramics. *Materials & Design* **122**, 307–314 (2017).

31. Lopes, D. V., Kovalevsky, A. V., Quina, M. J. & Frade, J. R. Electrochemical deposition of zero-valent iron from alkaline ceramic suspensions of $Fe_{2-x}Al_xO_3$ for iron valorisation. *Journal of The Electrochemical Society* vol. 167 102508 (2020).

32. Noble, B. B., Konovalova, A., Moutarlier, L. J., Brogden, V. & Kempler, P. A. Electrochemical chlor-iron process for iron production from iron oxide and salt water. *Joule* **8**, 714–727 (2024).

33. Öjefors, L. & Carlsson, L. An iron—air vehicle battery. *Journal of Power Sources* **2**, 287–296 (1978).

34. McKerracher, R., Ponce de Leon, C., Wills, R., Shah, A. & Walsh, F. C. A review of the iron–air secondary battery for energy storage. *ChemPlusChem* vol. 80 323–335 (2015).

35. Figueredo-Rodríguez, H. A. *et al.* A rechargeable, aqueous iron air battery with nanostructured electrodes capable of high energy density operation. *Journal of The Electrochemical Society* **164**, A1148 (2017).

36. Lee, D.-C., Lei, D. & Yushin, G. Morphology and phase changes in iron anodes affecting their capacity and stability in rechargeable alkaline batteries. *ACS Energy Letters* vol. 3 794–801 (2018).

37. Öjefors, L. SEM Studies of Discharge Products from Alkaline Iron Electrodes. *J. Electrochem. Soc.* **123**, 1691 (1976).

38. Öjefors, L. Temperature dependence of iron and cadmium alkaline electrodes. *Journal of the Electrochemical Society* **123**, 1139 (1976).

39. Sugimoto, T., Wang, Y., Itoh, H. & Muramatsu, A. Systematic control of size, shape and internal structure of monodisperse $\alpha\text{-}Fe_2O_3$ particles. *Colloids and Surfaces A: Physicochemical and Engineering Aspects* **134**, 265–279 (1998).

40. de Faria, D. L. A., Venâncio Silva, S. & de Oliveira, M. T. Raman microspectroscopy of some iron oxides and oxyhydroxides. *Journal of Raman Spectroscopy* **28**, 873–878 (1997).

41. Woodford, W. H., Chiang, Y.-M. & Carter, W. C. "Electrochemical Shock" of Intercalation Electrodes: A Fracture Mechanics Analysis. *J. Electrochem. Soc.* **157**, A1052 (2010).

42. Beaulieu, L. Y., Eberman, K. W., Turner, R. L., Krause, L. J. & Dahn, J. R. Colossal Reversible Volume Changes in Lithium Alloys. *Electrochem. Solid-State Lett.* **4**, A137 (2001).

43. Manohar, A. K. *et al.* Understanding the Factors Affecting the Formation of Carbonyl Iron Electrodes in Rechargeable Alkaline Iron Batteries. *Journal of The Electrochemical Society* vol. 159 A2148–A2155 (2012).

Supplementary Information for

Understanding the mechanism for the low-temperature reduction of Fe$_2$O$_3$ to Fe in alkaline electrolytes

Raj Shekhar,[1-2] Semanti Mukhopadhyay,[3] Francelia Sanchez,[3] Anastasiia Konovalova,[1–2] Shannon W. Boettcher,[1,2,4] Arun Devaraj,[3] Paul A. Kempler[1-2*]

[1]*Department of Chemistry and Biochemistry, University of Oregon, Eugene, OR, USA*
[2]*Oregon Center for Electrochemistry, University of Oregon, Eugene, OR, USA*
[3]*Physical and Computational Sciences Directorate, Pacific Northwest National Laboratory, Richland, WA, USA*
[4] *Department of Chemical & Biomolecular Engineering and Department of Chemistry, University of California, Berkeley, CA, USA*

*Correspondence: pkempler@uoregon.edu

Table of Contents

Supplementary Materials and Methods

Preparation of pc-Fe$_2$O$_3$

50 mL solution of 2M FeCl$_3$.6H$_2$O was prepared by completely dissolving 27.0 g of 2M FeCl$_3$·6 H$_2$O in DI water. The prepared solution was transferred into a 100 mL glass bottle with a stir bar. Another 50 mL solution of 5.4 M NaOH was prepared by mixing 21.6 g of 50 wt% NaOH and DI water. This newly prepared solution was added dropwise into the 2 M FeCl$_3$·6 H$_2$O solution while stirring constantly. The reaction mixture was allowed to stir for another 20 minutes before it was capped and placed in a preheated oven at 100 °C for 8 days.

After 8 days, the mixture was taken out and allowed to cool down at room temperature. The liquid solution at the top was decanted, and fresh DI water was added and the mixture was shaken well for 2 minutes. The mixture was allowed to rest so that the particles settled down. The supernatant was decanted again and the precipitate was removed from the bottle. The precipitate was transferred into the 50 mL centrifuge tube with DI water and the mixture was centrifuged at 7500 rpm for 15 minutes and the supernatant solution was decanted every time. The process was repeated 3–4 times to remove excess chloride ions. The precipitate was later dried under a vacuum at 60 °C overnight to obtain *pc*-Fe$_2$O$_3$.

Preparation of an-Fe$_2$O$_3$

Pseudocubic Fe$_2$O$_3$ particles were mixed in 1:1 (w/w) ratio with BaCl$_2$ and were transferred in an alumina container. This mixture was heated in a furnace at 1000 °C for 4 hours under a N$_2$ atmosphere. The mixture was taken out and allowed to cool down. Then the mixture was centrifuged with DI water at 7500 rpm for 15 minutes to remove BaCl$_2$. This process was repeated 3–4 times. The precipitate was then dried in a vacuum at 60 °C overnight to obtain *an*-Fe$_2$O$_3$.

Supplementary Table 1: Thermodynamic parameters at standard states. Thermodynamic parameters for iron, iron oxides and hydroxides at STP.

Chemical Species	ΔG^o (kJ/mol)	ΔH^o (kJ/mol)	ΔS^o (kJ/mol-K)
Fe_2O_3	−744.3	−718.37	0.087
Fe_3O_4	−1012.6	−969.09	0.146
Fe	0	8.05	0.027
$Fe(OH)_4^-$	−842.85	−829.44	0.045
$Fe(OH)_4^{2-}$	−775.9	−826.56	−0.17
$Fe(OH)_3$	−705.29	−673.48	0.106
$Fe(OH)_2$	−491.98	−465.74	0.088
OH^-	−157.29	−229.99	−0.244
H_2O	−237.14	−285.83	−0.163

Supplementary Table 2: Gibb's free energy at 80 °C. (Assuming ΔH^o and ΔS^o are temperature independent)

Chemical Species	$\Delta G_{80\,°C}$ (kJ/mol)
Fe_2O_3	−749.085
Fe_3O_4	−1020.63
Fe	−1.485
$Fe(OH)_4^-$	−845.325
$Fe(OH)_4^{2-}$	−766.55
$Fe(OH)_3$	−711.12
$Fe(OH)_2$	−495.84
OH^-	−143.87
H_2O	−228.175

Supplementary Table 3: Table of d-spacings for specific hkl planes observed from the SAED pattern of a *pc*-Fe$_2$O$_3$ particle.

2θ	*d*-spacing (Å) (from SAED)	hkl
24.15	3.69	012
33.16	2.72	104
35.63	2.53	110
39.90	2.18	113
57.47	1.67	116

Supplementary Table 4: Table of d-spacings for specific hkl planes observed from the SAED pattern of an *an*-Fe$_2$O$_3$ particle.

2θ	*d*-spacing (Å) (from SAED)	hkl
35.63	2.53	110
40.86	2.19	113
54.07	1.65	116
63.99	1.44	300
77.74	1.23	036

Supplementary Table 5: Calculated Fe atomic percentage and density predicted for various iron oxide phases.

Phase	Valency	Fe/(Fe+O) (at%)	Calculated Density (g cm^{-3})
α-Fe$_2$O$_3$	3	0.40	5.26
β-FeO(OH)	3	0.33	3.96
Fe$_3$O$_4$	2.33	0.43	5.17
FeO	2	0.50	5.70
Fe(OH)$_2$	2	0.50	3.84
α-Fe	0	1.00	7.87

Calculation of formal potential for Fe_2O_3 reduction to Fe metal

$Fe_2O_3(s) + 3\ H_2O + 6\ e^- \rightarrow 2\ Fe + 6\ OH^-(aq),$ 　　　　　　　　　　　　　**(S1)**
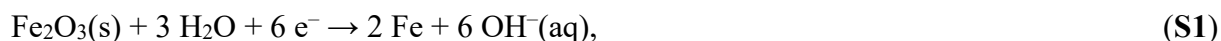
$\Delta G_{\ 80\ °C} = \Sigma n_p \Delta G_{product} - \Sigma n_r \Delta G_{reactant}$

　　$= (2\Delta G_{Fe} + 6\Delta G_{OH\text{-}}) - (\Delta G_{Fe2O3} + 3\Delta G_{H2O})$

　　$= 2(-1.485) + 6(-143.87) - (-749.085 + 3(-228.175))$

　　$= 567.42\ kJ/mol$

$E\ (vs\ SHE) = -\Delta G/nF$

　　　　$= -\ (567.2\ kJ/mol)/(6*96485\ C/mol)$

　　　　$= -\ 0.98\ V$

At pH = 15 and T = 80 °C,

$E\ (vs\ SHE) = -\ 0.98\ V - RT/nF*\Delta pH$

$E\ (vs\ SHE) = -\ 0.98\ V - 0.070$ 　　　(RT/nF = 70 mV at 80 °C)

　　　　$= -\ 1.05\ V$

Supplementary Discussion on RRDE measurements

During reductive sweep from –0.9 V to –1.3 V, when the ring potential was held at –1.1 V, sufficient to reduce any soluble Fe^{3+}, 5 μC was passed at the ring which corresponds to Fe^{3+} to Fe^{2+} reduction on the ring (**Fig. S20**). This correlates to 14 μC equivalent soluble Fe^{3+} is generated at the disk during the reduction, considering a collection efficiency of 36%. This amount corresponds to less than 0.1% of the total Fe^{3+} deposited at the disk in the first place. (Total charge passed is calculated by subtracting the baseline current of 0.011 A g^{-1}).

We thus attribute the lack of current in this region to a slower effective dissolution rate for *an*-Fe_2O_3 and/or inhibited dissolution in the presence of dissolved Fe^{3+}

The peak current in the Fe^0 region is ~3X the current observed for the $1e^-$ reduction of reactant ferric species.

Supplementary Discussion on the Dissolved Ferric/Ferrous Species

Previous X-ray absorption spectroscopy of ferric ions dissolved in 20 M NaOH support the presence of a single species in a tetrahedral coordination environment, $Fe(OH)_4^-$.[1] The reduced ferrous species has been most commonly reported as $Fe(OH)_3^-$,[2-6] but when $Fe(OH)_4^{2-}$ is included

in equilibrium calculations it is predicted to be the predominant dissolved ferrous species at $T \leq$ 100 °C.[7]

Supplementary Discussion on iron metal oxidation

In rotating ring-disk measurements, oxidation of Fe metal led to the formation of soluble Fe^{2+} species, which were detected when the ring was biased positively enough to oxidize Fe^{2+} to Fe^{3+}. The onset of Fe^{2+} formation was observed at $E > -1.0$ V (**Fig. S19a**). In the foregoing experiments, when the ring was biased negative ($E = -1.1$ V) , showed a reduction wave at the ring, $E > -0.95$ V, marking the formation of Fe^{3+} at the disk during iron metal oxidation (**Fig. S19b**). The oxidation of Fe^0 to Fe^{2+} onsets from $E = -1.0$ V and Fe^{2+} is not observed for $E > -0.8$ V. Similarly, the onset for oxidation of Fe^{2+} to Fe^{3+} occurs at $E = -0.95$ V and Fe^{3+} is not detected for $E > -0.68$ V, as depicted in (**Fig. S19c**).
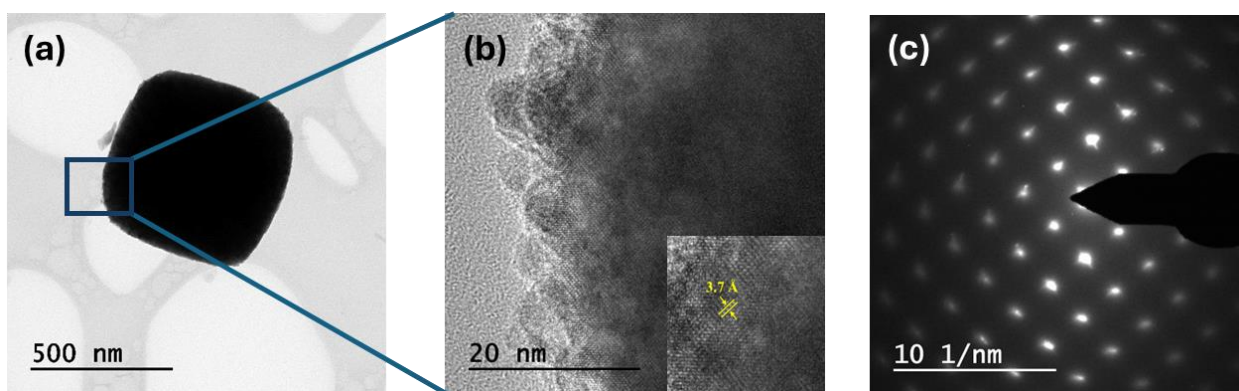
Figure S1: TEM images of *pc*–Fe_2O_3. (a) TEM image, (b) HRTEM image, inset showing the d-spacing between atomic fringes and (c) SAED pattern of *pc*-Fe_2O_3 and (d) table showing the d-spacing and the hkl plane observed from the SAED pattern.
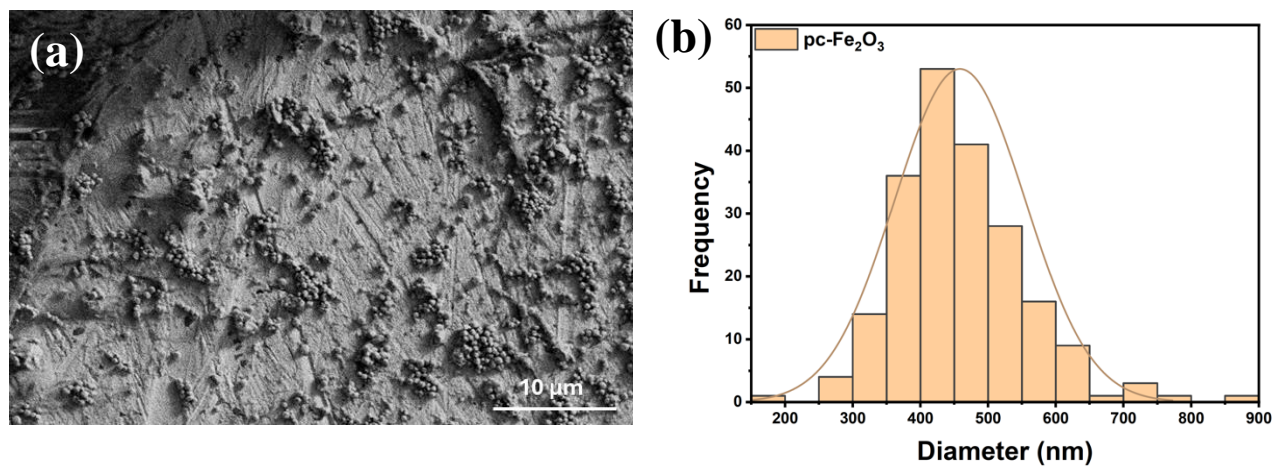
Figure S2: SEM image of *pc*-Fe$_2$O$_3$. (a) SEM image (b) Distribution of *pc*-Fe$_2$O$_3$ diameters.
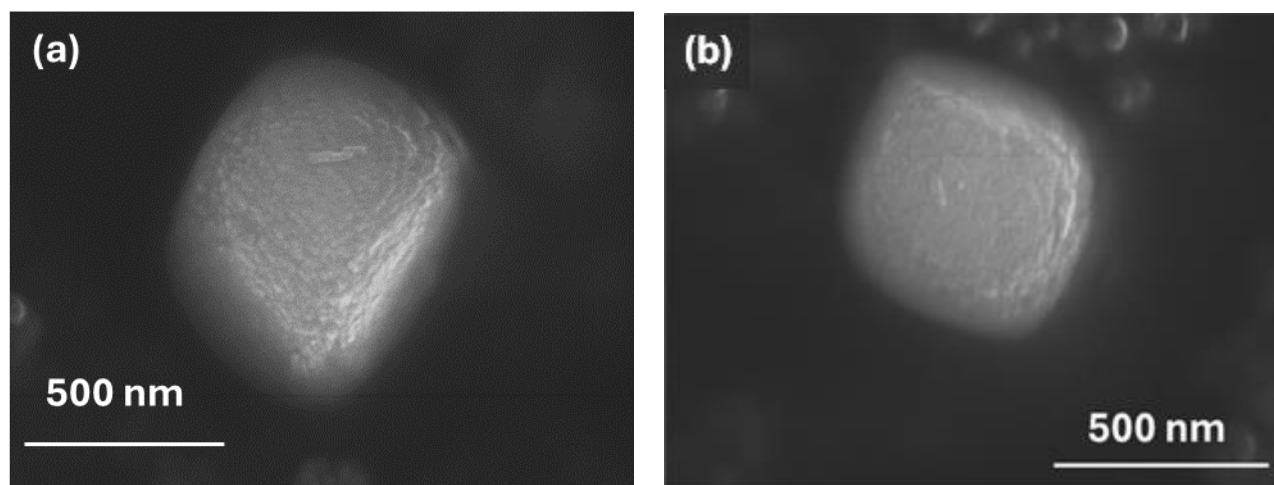
Figure S3: SEM images of *pc*-Fe$_2$O$_3$.
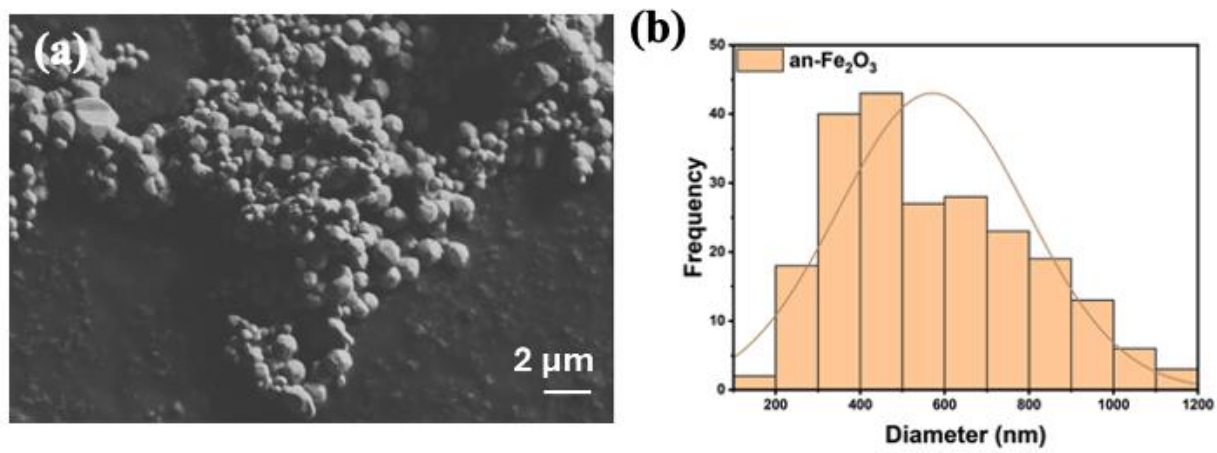
Figure S4: SEM image of *an*-Fe$_2$O$_3$. (a) SEM image (b) Distribution of *an*-Fe$_2$O$_3$ diameters.
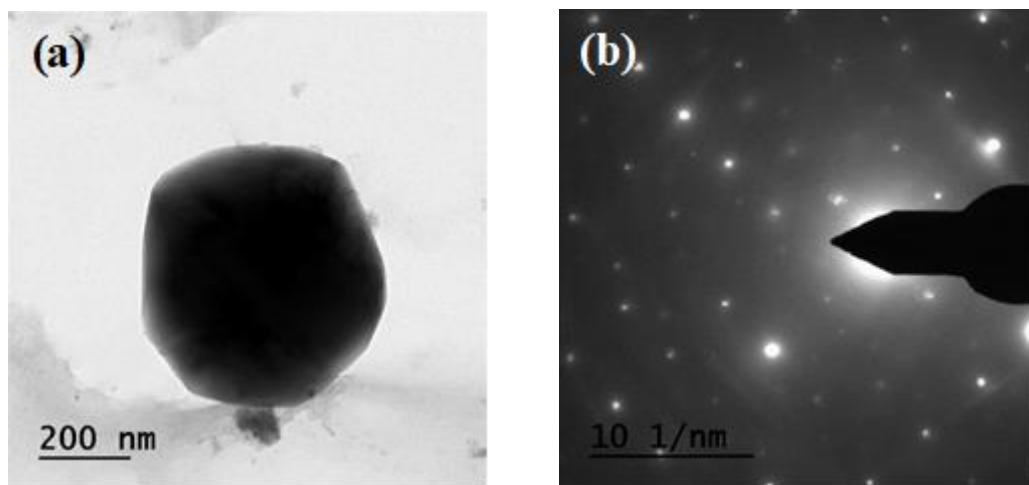
Figure S5: TEM images of *an*-Fe$_2$O$_3$. (a) TEM image, (b) SAED pattern of *an*-Fe$_2$O$_3$, and (c) table showing the d-spacing and the hkl plane observed from the SAED pattern.
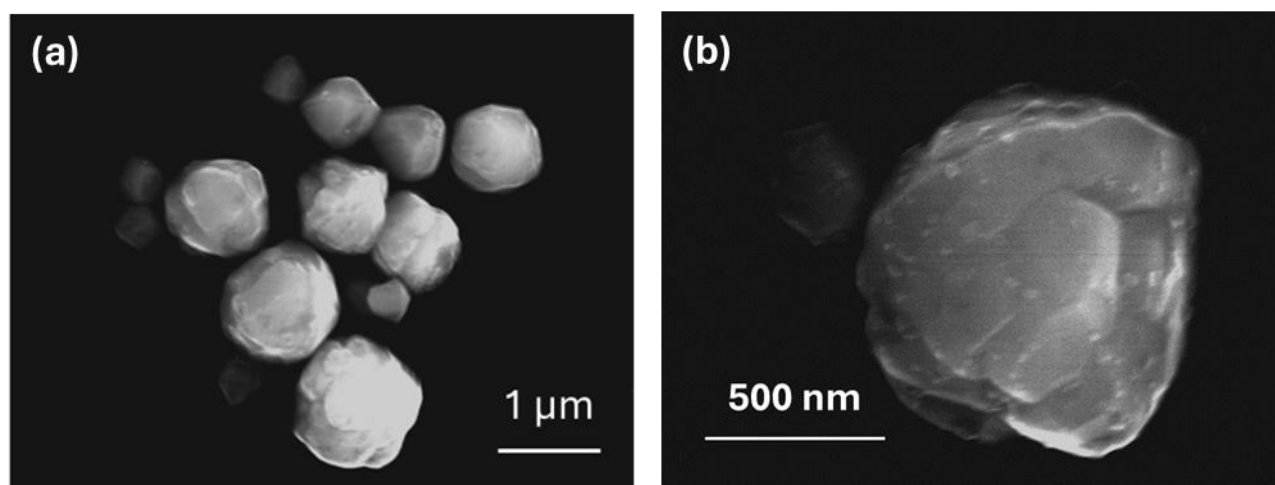
Figure S6: SEM images of *an*-Fe$_2$O$_3$.
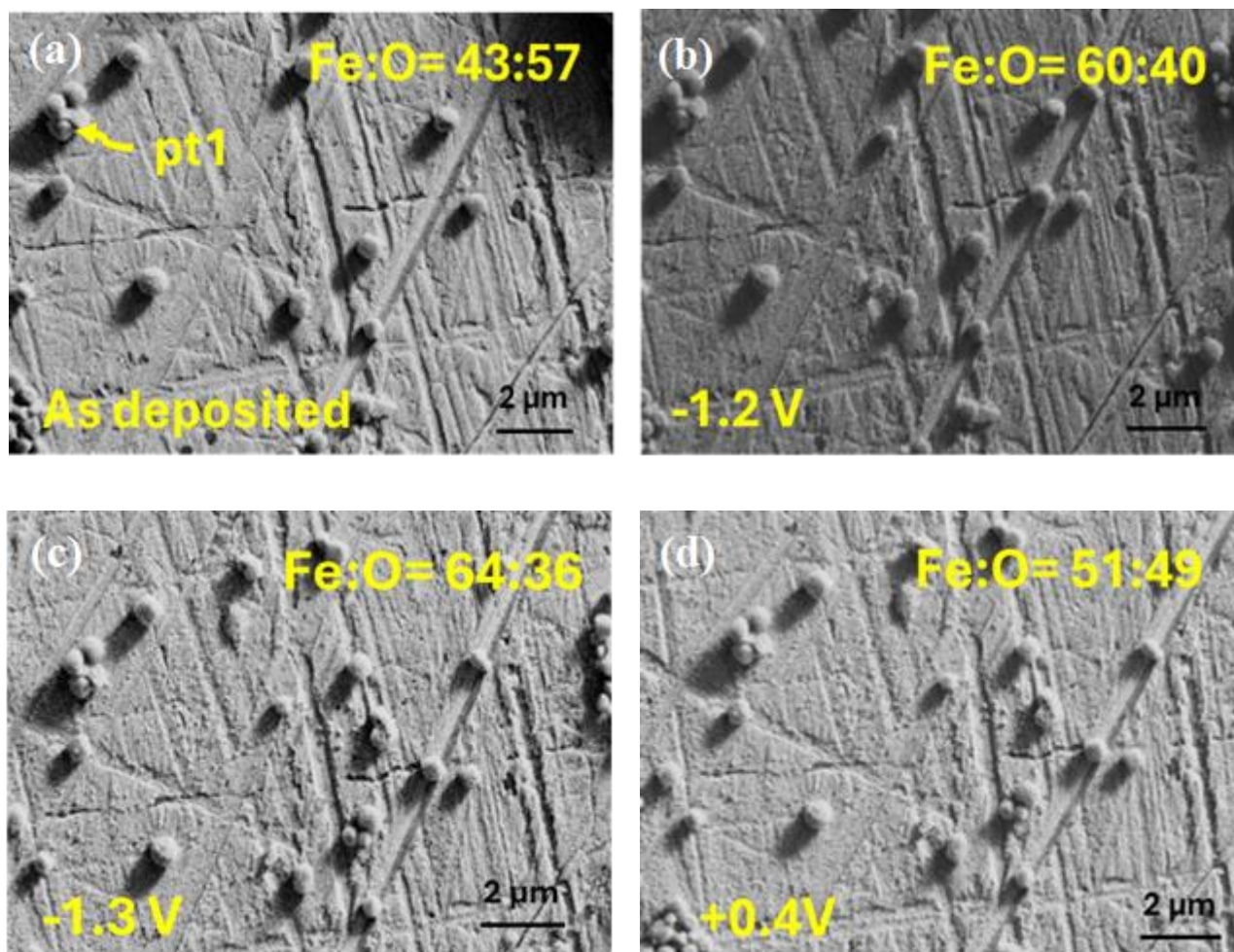
Figure S7: Correlated ex-situ SEM images of *pc*-Fe$_2$O$_3$ before and after reduction (a–d). Fe$_2$O$_3$ particles were drop cast at 43 µg cm^{-2} onto the Au electrode and dried in air before imaging. A constant potential (indicated at the left bottom corner) was applied to reduce the particles for 5 minutes. The Fe and O ratio is depicted at the top for the site (pt1).
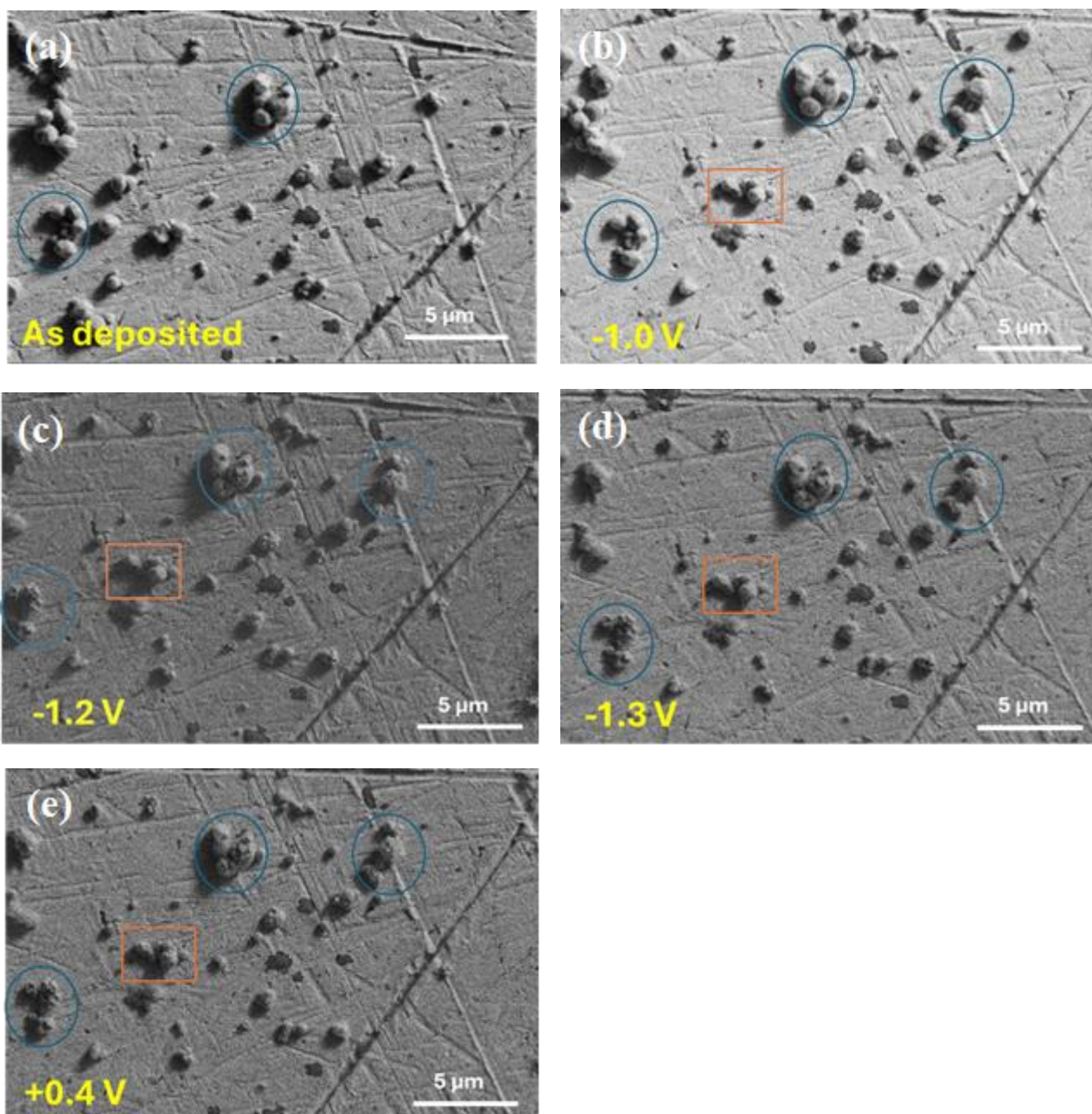
Figure S8: Correlated ex-situ SEM images of *an*-Fe_2O_3 before and after reduction (a–e). Fe_2O_3 particles were drop cast at 43 µg cm^{-2} onto the Au electrode and dried in air before imaging. A constant potential (indicated at the left bottom corner) was applied to reduce the particles for 5 minutes.
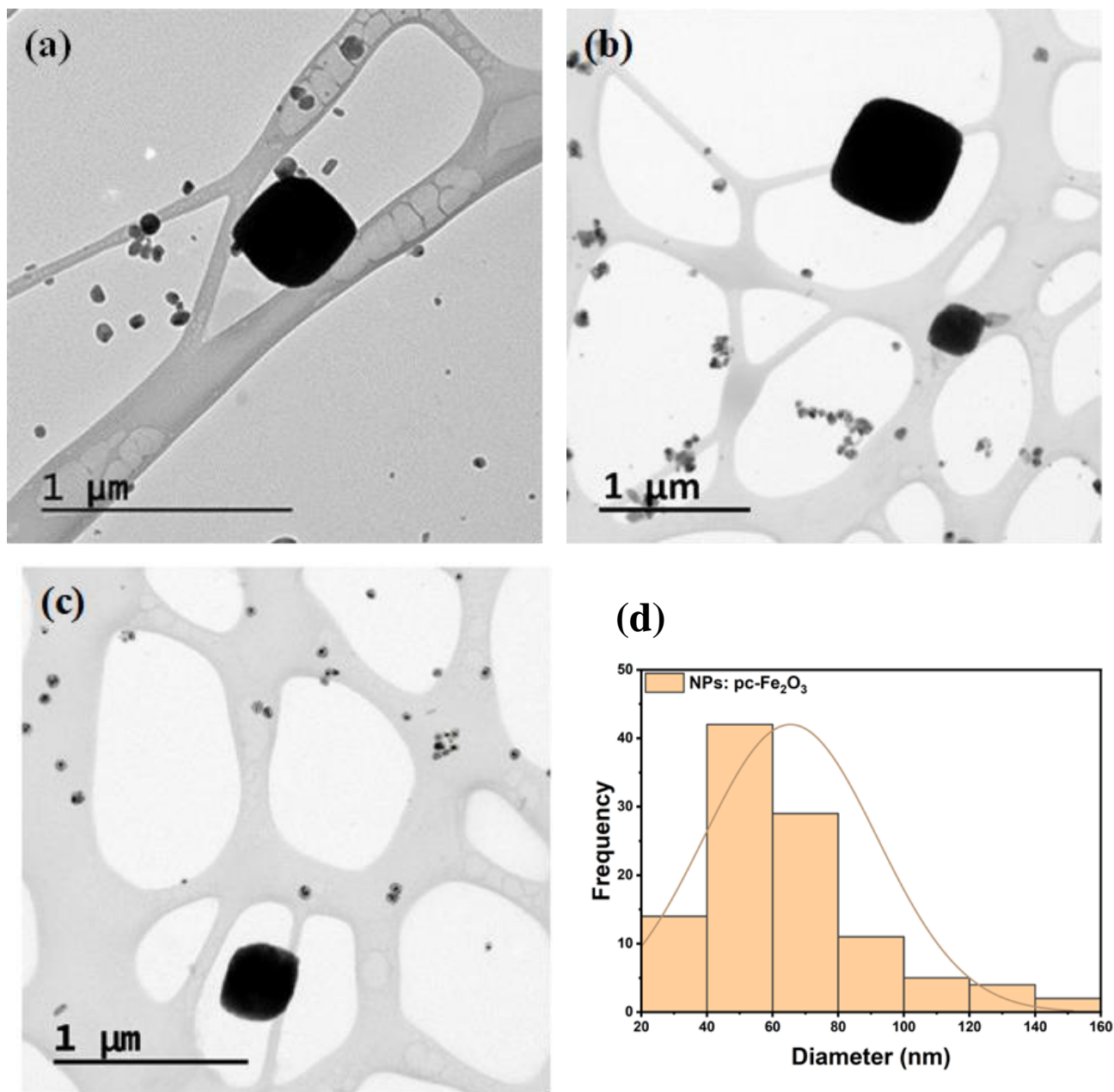
Figure S9: Post-reduction TEM images of *pc*-Fe₂O₃ (a, b, c). (d) Distribution of newly formed nanoparticles in *pc*-Fe₂O₃ from the TEM image from three data sets. Fe₂O₃ particles were drop cast on the Cu TEM grid, serving as the working electrode during reduction.
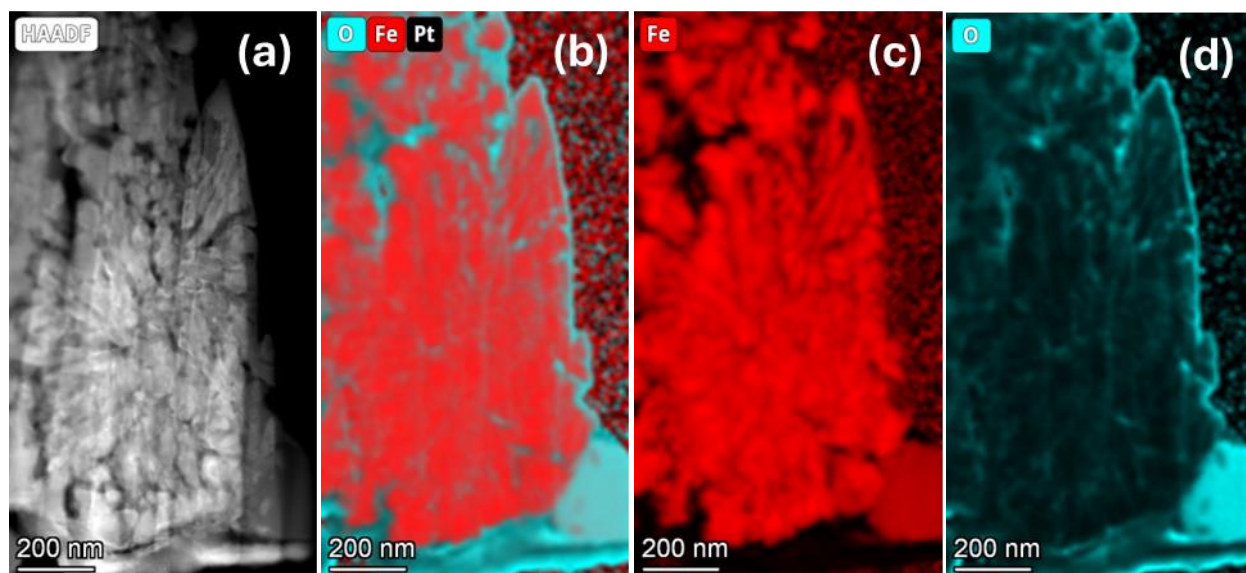
Figure S10: TEM-EDX images of a cross-section of a fractured *an*-Fe$_2$O$_3$. (a) Darkfield TEM image of the cross-section. (b,c,d) EDX mapping of the cross-section showing the content of oxygen and iron.
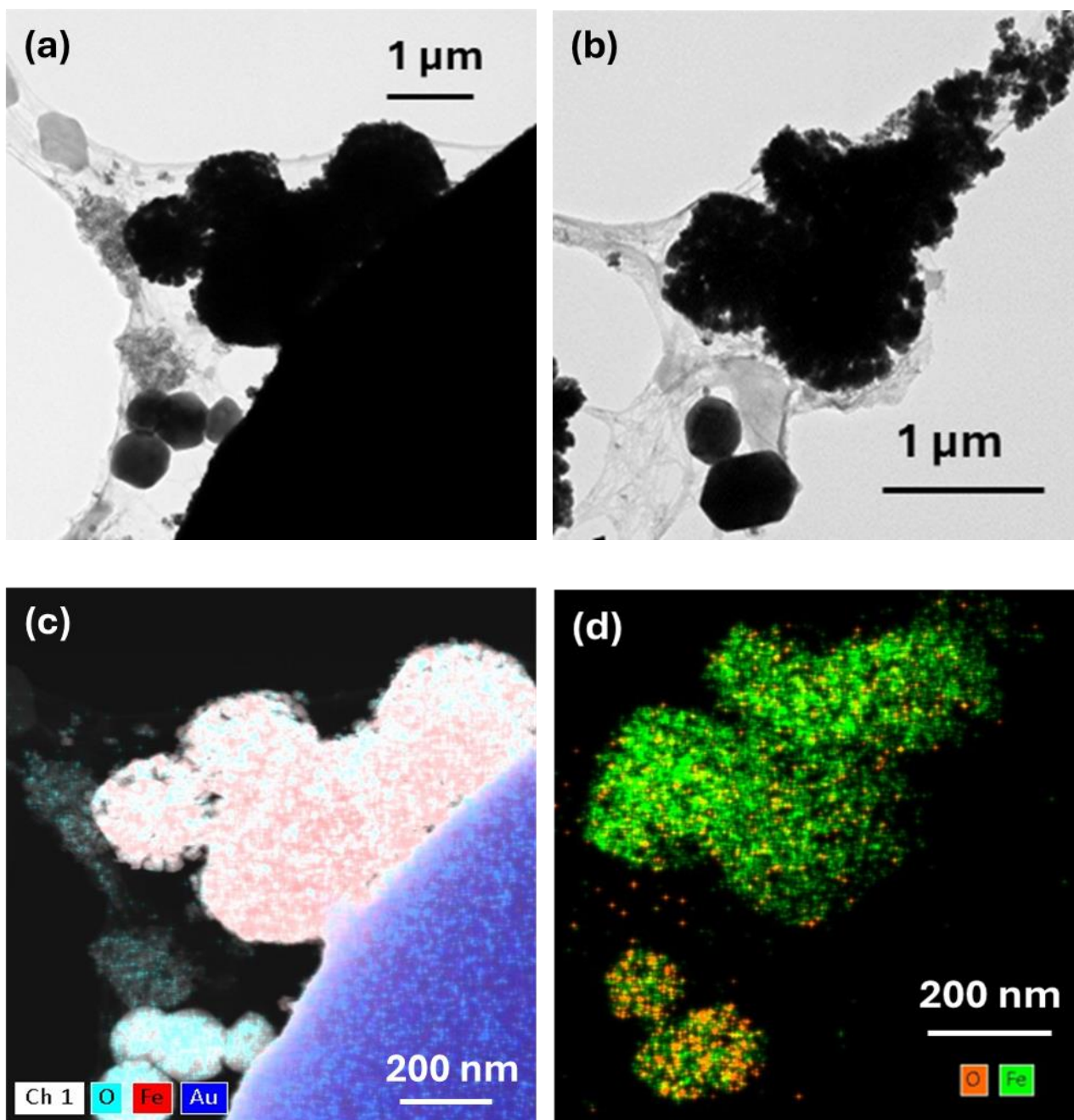
Figure S11: TEM images of *an*-Fe$_2$O$_3$ post reduction. (a,b) TEM images of two different sites. (c,d) TEM-EDX of (a) and (b), respectively.
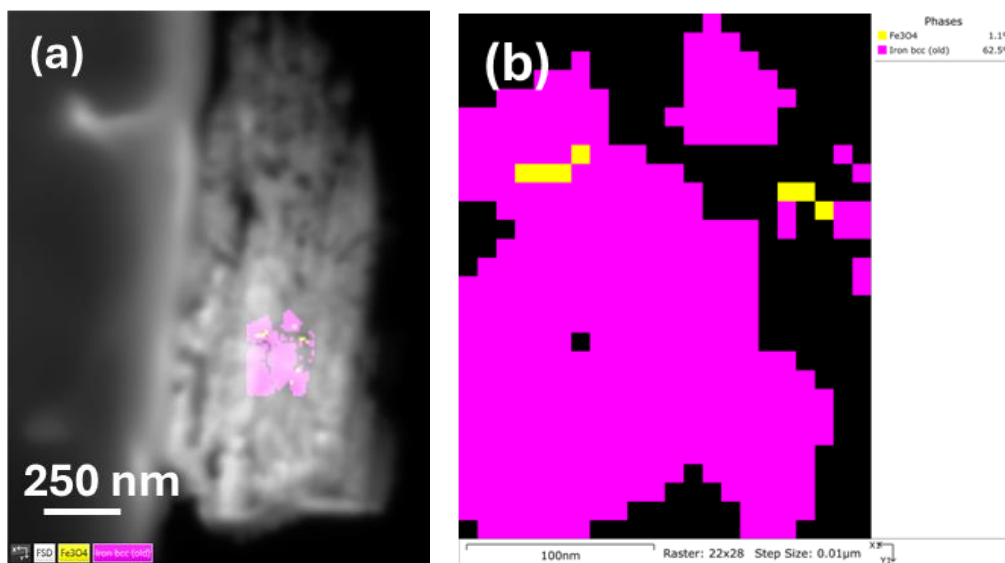
Figure S12: TKD of the center of the fractured particle.
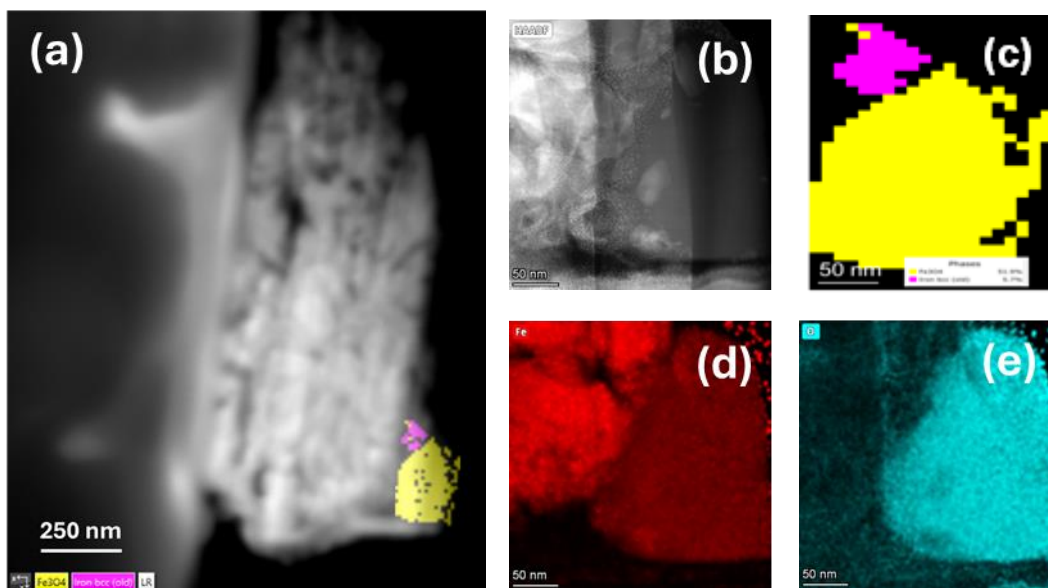
Figure S13: EDX and TKD of unfractured particle. (a) HAADF image. (b) STEM image. (c) TKD. (d,e) EDX mapping.
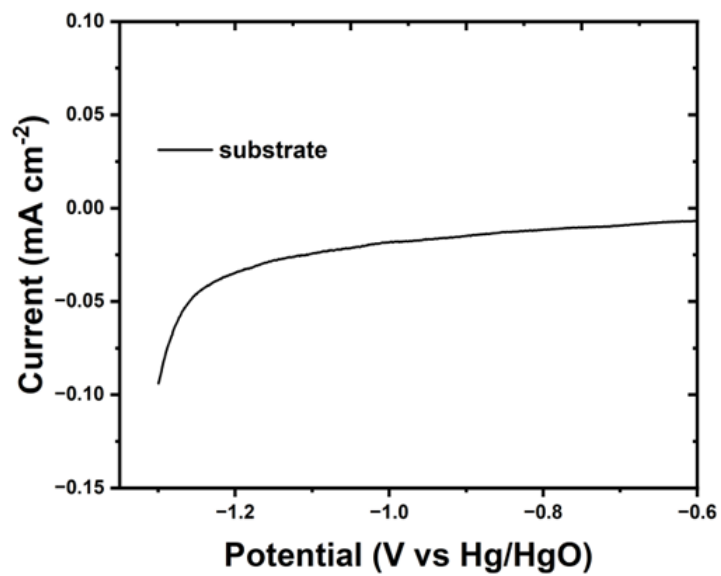
Figure S14: Voltametric scan for a glassy carbon working electrode in 30 wt.% NaOH at 80 °C.
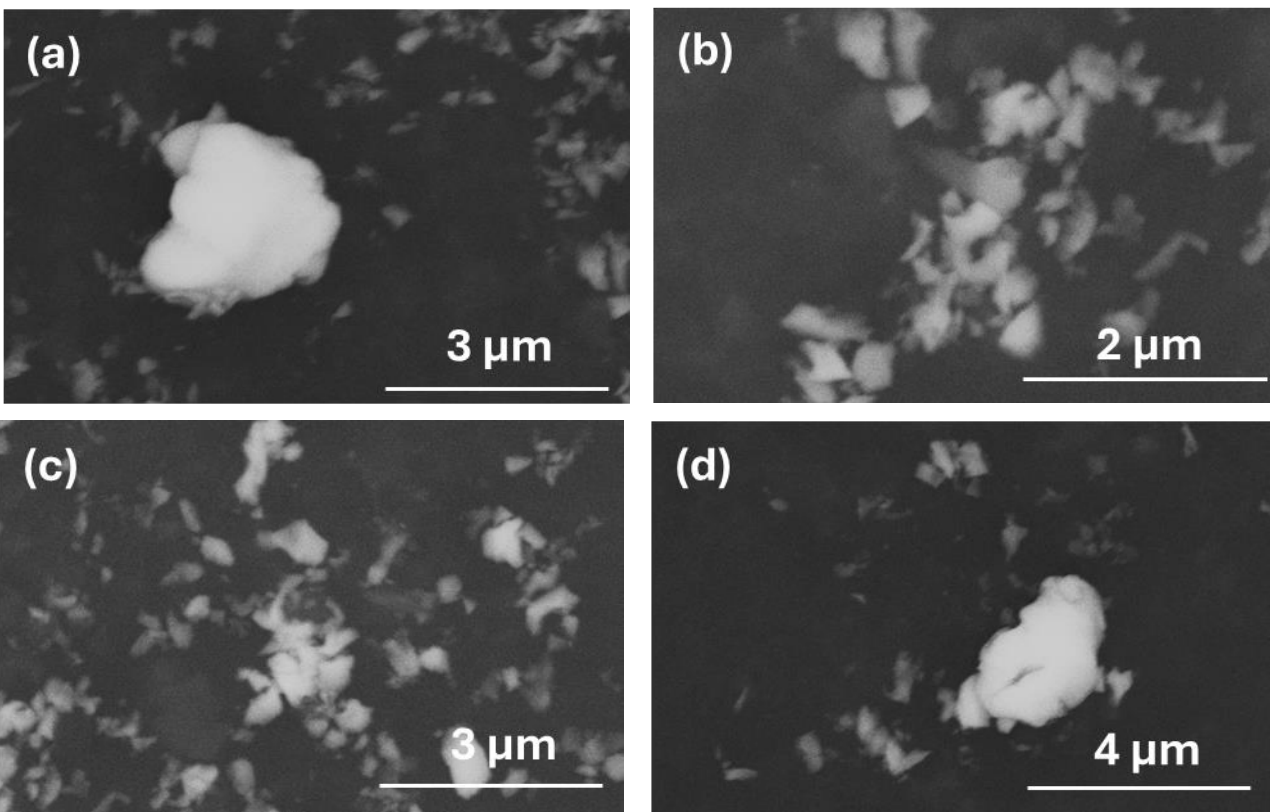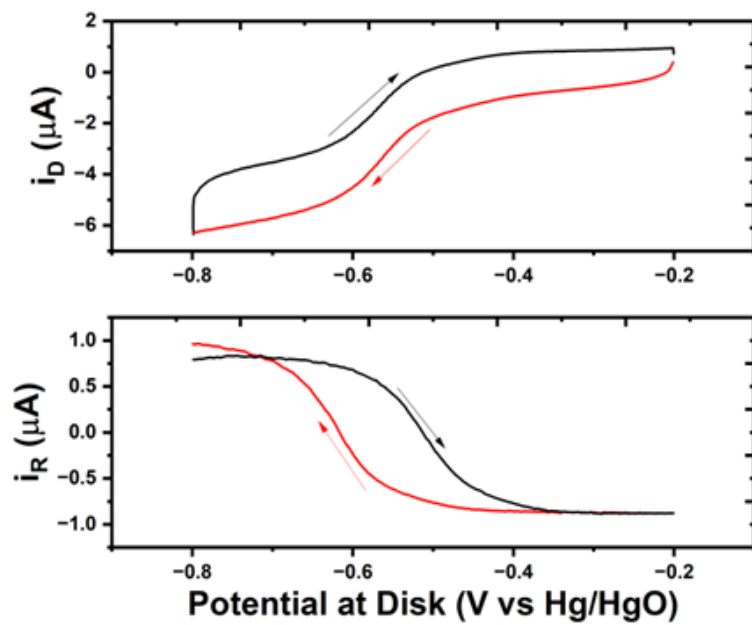
Figure S15: SEM images of *nat*-Fe$_2$O$_3$.

Figure S16: Collection efficiency of the glassy-carbon RRDE in 30 wt% NaOH at 80 °C measured with a 1 mM $[RuCl_3]^{2+/3+}$ redox couple.
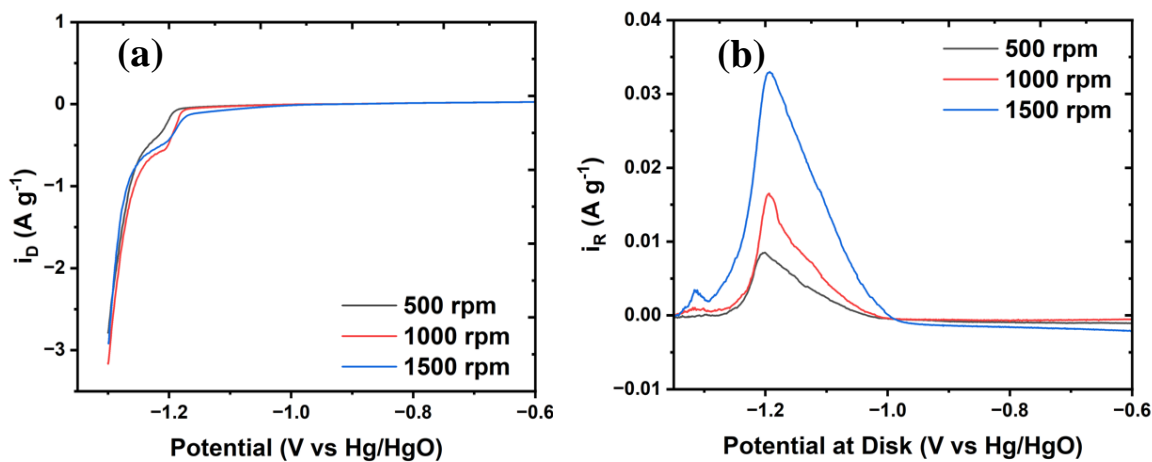
Figure S17: Rate of dissolution of *pc*-Fe$_2$O$_3$. 5 µg *pc*-Fe$_2$O$_3$ was deposited on the disk of RRDE. Scan rate = 5 mV s–1. Rotation rate = 1000 rpm. The ring's potential was held at –0.3 V vs Hg/HgO. The initial Fe$_2$O$_3$ deposited on the disk of RRDE was 70 µg cm^{-2}.

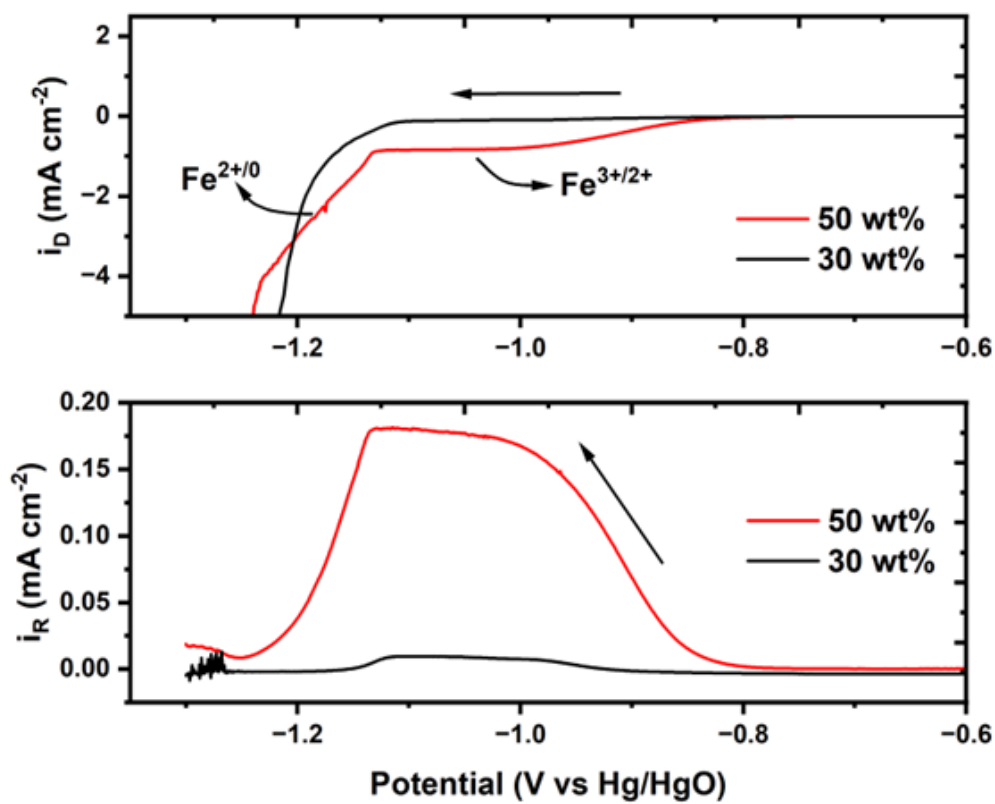**Figure S18:** RRDE of *com*-Fe_2O_3 slurry (~7 wt.%) in 30 wt.% NaOH and 50 wt.% NaOH at 80 °C showing reductive sweep at $v = 5$ mV s^{-1}. The ring's potential was held at –0.3 V vs Hg/HgO.
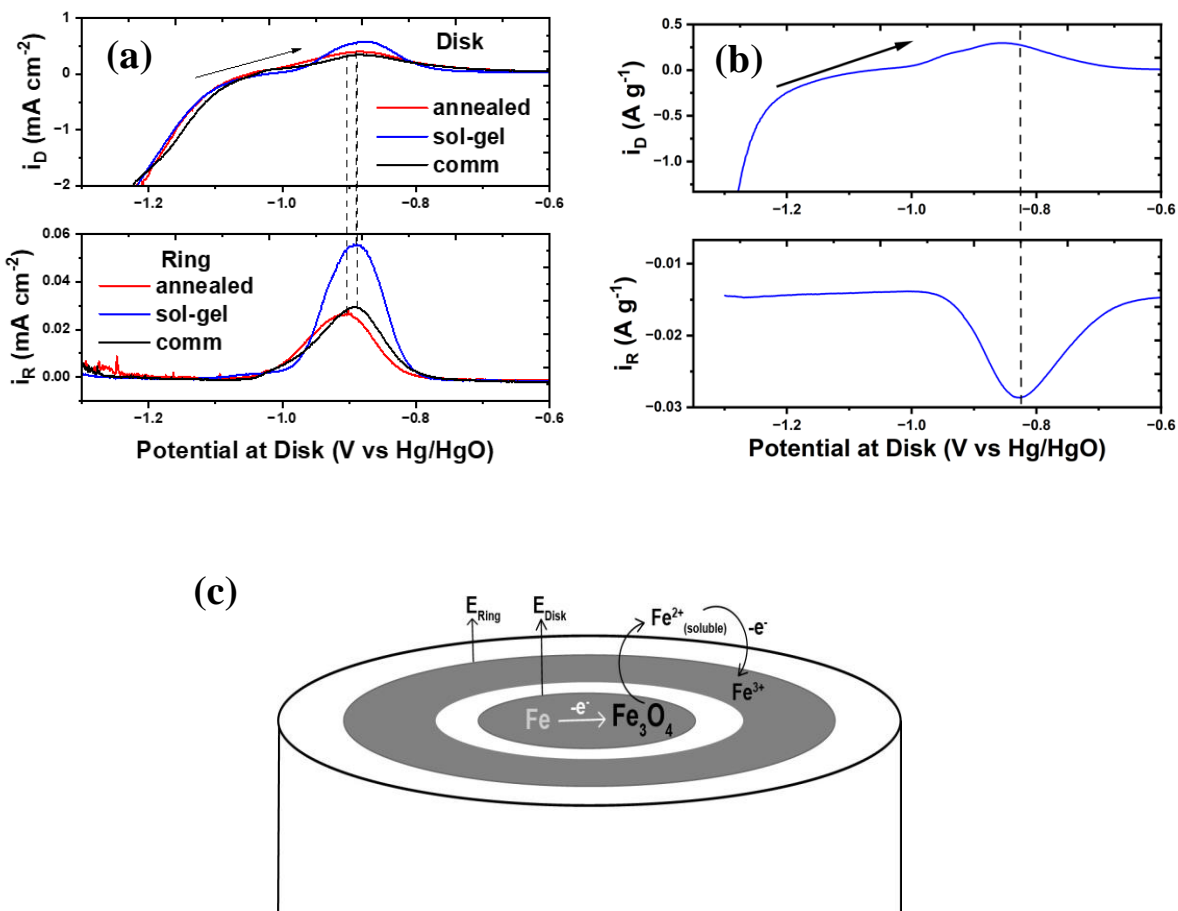
Figure S19: Oxidation cycle of various hematite samples. Thin film RRDE of glassy carbon electrodes modified with thin films in 30 wt% NaOH at 80 °C showing (a) full oxidative sweep of *com*-Fe_2O_3, *pc*-Fe_2O_3 and *an*-Fe_2O_3 keeping the ring potential fixed at -0.3 V with a scan rate = 5 mV s^{-1} and rotation rate = 1000 rpm. The initial loading of Fe_2O_3 deposited on the disk of RRDE was 42.6 µg cm^{-2}. (b) oxidative sweep of *pc*-Fe_2O_3 with the ring potential held at -1.1 V. (c) Scheme of the oxidation of Fe metal at the disk on RRDE.
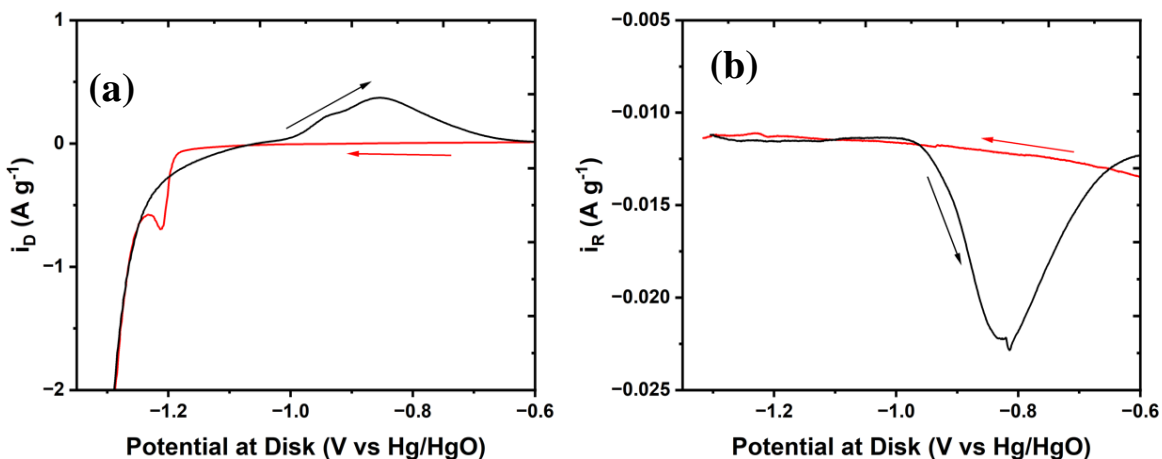
Figure S20: Presence of soluble ferric species during iron metal oxidation using RRDE. Thin film RRDE of glassy carbon electrodes modified with thin films of *pc*-Fe$_2$O$_3$ in 30 wt% NaOH at 80 °C showing (a) full voltammetry cycle, (b) reductive sweep at lower currents. Scan rate = 5 mV s^{-1}. Rotation rate = 1000 rpm. The ring's potential was held at –1.1 V vs Hg/HgO. Total Fe$_2$O$_3$ deposited on the disk of RRDE equals 70 µg cm^{-2}.
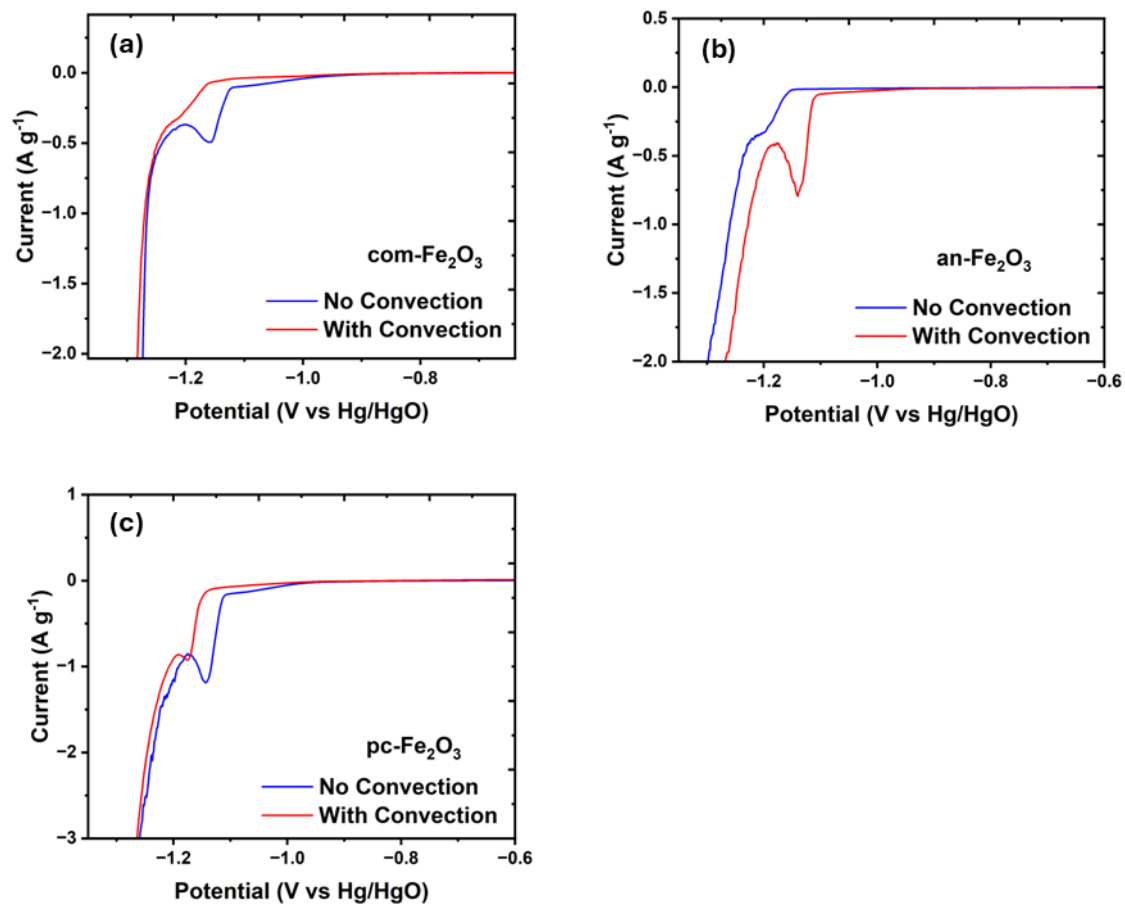
Figure S21: Comparison of voltammetry with and without convection. (a) *com*-Fe$_2$O$_3$ (b) *an*-Fe$_2$O$_3$ and (c) *pc*-Fe$_2$O$_3$.

Supplementary References

(1) Sipos, P.; Zeller, D.; Kuzmann, E.; Vértes, A.; Homonnay, Z.; Walczak, M.; Canton, S. E. The structure of Fe (III) ions in strongly alkaline aqueous solutions from EXAFS and Mössbauer spectroscopy. *Dalton Transactions* **2008**, (41), 5603-5611.

(2) Majid, A. I.; Finotello, G.; van der Schaaf, J.; Deen, N. G.; Tang, Y. On the formation of dendritic iron from alkaline electrochemical reduction of iron oxide prepared for metal fuel applications. *Chemical Engineering Science* **2024**, *291*, 119931.

(3) Allanore, A.; Lavelaine, H.; Valentin, G.; Birat, J.; Delcroix, P.; Lapicque, F. Observation and modeling of the reduction of hematite particles to metal in alkaline solution by electrolysis. *Electrochimica Acta* **2010**, *55* (12), 4007-4013.

(4) Zou, X.; Gu, S.; Lu, X.; Xie, X.; Lu, C.; Zhou, Z.; Ding, W. Electroreduction of iron (III) oxide pellets to iron in alkaline media: a typical shrinking-core reaction process. *Metallurgical and Materials Transactions B* **2015**, *46*, 1262-1274.

(5) Zou, X.; Gu, S.; Cheng, H.; Lu, X.; Zhou, Z.; Li, C.; Ding, W. Facile electrodeposition of iron films from $NaFeO_2$ and Fe_2O_3 in alkaline solutions. *Journal of The Electrochemical Society* **2014**, *162* (1), D49.

(6) Allanore, A.; Lavelaine, H.; Valentin, G.; Birat, J.; Lapicque, F. Electrodeposition of metal iron from dissolved species in alkaline media. *Journal of the Electrochemical Society* **2007**, *154* (12), E187.

(7) Beverskog, B.; Puigdomenech, I. Revised pourbaix diagrams for iron at 25–300 C. *Corrosion Science* **1996**, *38* (12), 2121-2135.